Space Sci Rev (2010) 154: 219–251
DOI 10.1007/s11214-010-9652-0

Lunar Magnetic Field Observation and Initial Global Mapping of Lunar Magnetic Anomalies by MAP-LMAG Onboard SELENE (Kaguya)

Hideo Tsunakawa · Hidetoshi Shibuya · Futoshi Takahashi · Hisayoshi Shimizu · Masaki Matsushima · Ayako Matsuoka · Satoru Nakazawa · Hisashi Otake · Yuichi Iijima

Received: 27 August 2009 / Accepted: 7 April 2010 / Published online: 4 May 2010
© Springer Science+Business Media B.V. 2010

Abstract The magnetic field around the Moon has been successfully observed at a nominal altitude of ∼100 km by the lunar magnetometer (LMAG) on the SELENE (Kaguya) spacecraft in a polar orbit since October 29, 2007. The LMAG mission has three main objectives: (1) mapping the magnetic anomaly of the Moon, (2) measuring the electromagnetic and plasma environment around the Moon and (3) estimating the electrical conductivity structure of the Moon. Here we review the instrumentation and calibration of LMAG and report the initial global mapping of the lunar magnetic anomaly at the nominal altitude. We have applied a new de-trending technique of the Bayesian procedure to multiple-orbit datasets observed in the tail lobe and in the lunar wake. Based on the nominal observation of 14 months, global maps of lunar magnetic anomalies are obtained with 95% coverage of the lunar surface. After altitude normalization and interpolation of the magnetic anomaly field by an inverse boundary value problem, we obtained full-coverage maps of the vector magnetic field at 100 km altitude and the radial component distribution on the surface. Relatively strong anomalies are identified in several basin-antipode regions and several near-basin and near-crater regions, while the youngest basin on the Moon, the Orientale basin, has no magnetic anomaly. These features well agree with characteristics of previous maps based on the

H. Tsunakawa (✉) · F. Takahashi · M. Matsushima
Department of Earth and Planetary Sciences, Tokyo Institute of Technology, Tokyo 152-8551, Japan
e-mail: htsuna@geo.titech.ac.jp

H. Shibuya
Department of Earth and Environmental Sciences, Kumamoto University, Kumamoto 860-8555, Japan

H. Shimizu
Earthquake Research Institute, University of Tokyo, Tokyo 113-0032, Japan

A. Matsuoka · Y. Iijima
Institute of Space and Astronautical Science, Japan Aerospace Exploration Agency, Sagamihara, Kanagawa 252-5210, Japan

S. Nakazawa · H. Otake
Lunar and Planetary Exploration Program Group, Japan Aerospace Exploration Agency, Tsukuba, Ibaraki 305-8505, Japan

Lunar Prospector observation. Relatively weak anomalies are distributed over most of the lunar surface. The surface radial-component distribution estimated from the inverse boundary value problem in the present study shows a good correlation with the radial component distribution at 30 km altitude by Lunar Prospector. Thus these weak anomalies over the lunar surface are not artifacts but likely to be originated from the lunar crustal magnetism, suggesting possible existence of an ancient global magnetic field such as a dynamo field of the early Moon. The possibility of the early lunar dynamo and the mechanism of magnetization acquisition will be investigated by a further study using the low-altitude data of the magnetic field by Kaguya.

Keywords Moon · Kaguya · Magnetic field · Magnetic anomaly · Crustal magnetization · Dynamo

1 Introduction

Lunar magnetism has been investigated by satellites, ground survey and returned samples for the last several decades concerning three main targets: (1) crustal magnetic fields of the Moon, (2) electromagnetic and plasma environment around the Moon and (3) electrical conductivity structure of the Moon. It is well known that the Moon has no global magnetic field, unlike the Earth, rather it has significantly strong crustal magnetic anomalies (e.g. Coleman et al. 1972; Hood et al. 1981; Richmond and Hood 2008; Mitchell et al. 2008). The origin of magnetic anomalies is one of the most important and debatable issues of lunar science. For the lunar electromagnetic and plasma environment, the main controlling factor is interaction between the Moon and the solar wind plasma. The Moon without global magnetic fields in the solar wind results in generating a tail-like plasma void called the lunar wake (Lyon et al. 1967). This provides a good opportunity to study the behavior of the solar wind behind an unmagnetized solid body. For a smaller scale interaction, there may be a small magnetosphere over the crustal magnetic anomaly, called the mini-magnetosphere (e.g. Lin et al. 1998; Kurata et al. 2005; Halekas et al. 2008). When shock waves of the solar wind pass through the Moon, and when the Moon moves into the Earth's magnetosphere, the induced field is observed as a transient field (e.g. Dyal et al. 1974; Hood et al. 1999). Most important is the estimate of the metallic core size, which gives a crucial constraint on the Moon's formation with respect to the giant impact hypothesis of the Earth-Moon system (Hartmann and Davis 1975). According to the giant impact hypothesis, the rocky material accumulated at an orbit of the Roche limit formed the Moon, and thus the lunar metallic core should be small. This is directly relevant to a possible lunar dynamo and the origin of the lunar magnetic anomaly. However, it is not easy to obtain an accurate structure of the electrical conductivity since induced fields are very small (<1 nT).

Lunar magnetic anomalies were observed by the magnetometer on the Apollo 15 and 16 subsatellites (e.g. Coleman et al. 1972; Hood et al. 1981). They are distributed as spots of the order of 100 km in horizontal scale, showing intensity of a few nano-tesla at $\sim$100 km altitude. Magnetization of the lunar crust was also indicated by surface magnetometer measurements (e.g. Dyal et al. 1974). While the Apollo observations were limited to the low-to-middle latitude band (35° N–35° S), the magnetic field measurement by the Lunar Prospector (LP) spacecraft in a polar orbit covered almost the entire lunar surface and then provided the in-situ vector field by the magnetometer (Hood et al. 2001) and the lunar surface intensity by the electron reflectometer (Lin et al. 1998; Halekas et al. 2001). Based on the LP data, the preliminary global maps have been

reported for the vector field at 30 and 40 km altitudes (Richmond and Hood 2008; Purucker 2008) and for the lunar surface intensity (Mitchell et al. 2008). The LP mapping results indicate that there are more anomalies on the lunar surface, and it is suggested from the LP and Apollo missions that strong anomalies tend to be distributed on antipodes of the lunar basins (e.g. Lin et al. 1988, 1998; Hood et al. 2001; Halekas et al. 2001).

It is generally accepted that the lunar magnetic anomalies originated from natural remanent magnetization of the lunar crust acquired in a certain ambient magnetic field. However, the origin of lunar magnetic anomalies has been debated. From paleomagnetic studies of the returned lunar rocks, their magnetizations are thought to be thermoremanent and/or shock remanent in some ambient field (e.g. Fuller 1974). For the ambient field, two major sources have been proposed so far: one is the interplanetary magnetic field enhanced by plasma due to the basin-forming impact (e.g. Hood and Vickery 1984; Lin et al. 1988; Hood and Artemieva 2008) or the magnetic field of a comet amplified by its impact (e.g. Schultz and Srnka 1980), and the other is the global magnetic field generated by ancient lunar dynamo (e.g. Runcorn 1983; Hood and Artemieva 2008). In the latter case, it gives a crucial constraint on the Moon's thermal evolution and the structure of the lunar deep interior (e.g. Stegman et al. 2003). Although lunar paleointensity data have been controversial, a recent experimental study of the returned lunar rocks suggests that the lunar magnetic field intensity was $\sim$1 μT about 4.2 billion years ago (Garric-Bethell et al. 2009). This may be supported by the recent study of numerical dynamo simulation of the early Moon (Takahashi and Tsunakawa 2009). If the lunar dynamo worked once, it may have affected formation and evolution of the early Earth's atmosphere by a possible lunar magnetosphere (Takahashi and Tsunakawa 2009).

Lunar MAGnetometer (LMAG) of the magnetic field and plasma experiment (MAP) onboard the SELENE (Kaguya) spacecraft was designed for precise observation of the vector magnetic field around the Moon. In this paper we review instrumentation and calibration of LMAG and report the initial global mapping results of the lunar magnetic anomaly at a nominal altitude of $\sim$100 km. Electromagnetic and plasma environment around the Moon was observed in collaboration with Plasma energy Angle and Composition Experiment (PACE), and the initial results have been reported (e.g. Saito et al. 2008b; Nishino et al. 2009a, 2009b; Yokota et al. 2009; Nagai et al. 2009; Tanaka et al. 2009). The electron reflectometry of the lunar magnetic anomaly has been conducted in collaboration with PACE, and the initial global mapping results will be provided (Saito et al. 2008c; Yamamoto et al., in preparation). Electrical conductivity structure of the Moon has been analyzed and will be reported elsewhere (Shimizu et al., in preparation).

2 Instrumentation and Calibration

2.1 Instrumentation

LMAG, with a triaxial ring-core type fluxgate sensor (MGF-S), was designed on the basis of magnetometers of two previous missions, Geotail (Kokubun et al. 1994) and Nozomi (Yamamoto and Matsuoka 1998). The noise level of peak-to-peak is less than 0.1 nT, and basic specification of LMAG is summarized in Table 1.

MGF-S has four dynamic ranges of ±64, ±256, ±1024 and ±65536 nT with a resolution of 16 bits and a linearity better than 0.1% (Shimizu et al. 2008). Sampling rate is 32 Hz with a low-pass filter of 10 Hz cut frequency. MGF-S was mounted on the top plate of a 12 m-long mast to avoid possible magnetic interferences of the spacecraft. The mast was

Table 1 Basic specification of LMAG

Sensor of MGF-S	three ring-core sensors
Linearity	better than 10^{-3}
Dynamic range	range-3 : ±65536 nT
	range-2 : ±1024 nT
	range-1 : ±256 nT
	range-0 : ±64 nT
Resolution	range-3 : 2.0 nT
(16 bit)	range-2 : 0.03 nT
	range-1 : 0.008 nT
	range-0 : 0.002 nT
Noise level	less than 0.1 nT
(peak-to-peak)	
Sampling rate	32 Hz
Mast	12 m in length
Canister	0.9 m in length,
	0.3 m in diameter
Mass of sensor system	14 kg in total
(including SAM-C)	
Control unit, MAP-E	9 kg in total,
(including PACE)	76 W in nominal

initially stowed in a canister (0.9 m in length and 0.3 m in diameter), and deployed after the spacecraft was inserted into a polar orbit at a nominal altitude of ∼100 km. Sensor alignment was first calibrated in the ground test (Fig. 1) and finally determined in orbit with known fields, 1 Hz triangle waves of 2.6 nT peak-to-zero amplitude at the MGF-S position. This calibration field is generated by two coil systems (SAM-C, Sensor Alignment Monitor Coil) which were wound around a fiber-reinforced-plastic cylinder inside the canister. The mass of the LMAG sensor system is 14 kg in total. Details of the sensor alignment determination are described by Shimizu et al. (2008) and Takahashi et al. (2009).

Magnetic interference from each of the mission instruments and the bus devices was carefully measured and improved to satisfy the electromagnetic compatibility (EMC) condition of the magnetic field (DC < 0.06 nT, AC < 0.002 nT) at the MGF-S position in the ground test. It was confirmed from summing up each measurement that magnetic interference in total was negligible at the sensor position. After the spacecraft began to orbit around the Moon at the nominal altitude, LMAG was first deployed and turned on. Subsequently the interference field was checked for each mission instrument in the initial check-out phase. Details of the EMC control are reported by Matsushima et al. (2010).

Control units of MGF-S, mast, telemetry-command and house-keeping were contained in an aluminum alloy box (MAP-E) together with power supply and PACE control units. MAP-E has a mass of 9 kg and a power consumption of 76 W at nominal operation of both LMAG and PACE. Details of PACE specification are described by Saito et al. (2008a, 2010).

2.2 Calibration

Linearity and orthogonality of three ring-core sensors of MGF-S and the SAM-C field were calibrated in the ground test (Shimizu et al. 2008). In-orbit calibrations were carried out for sensor alignment and zero offsets extensively during the initial check-out phase, October

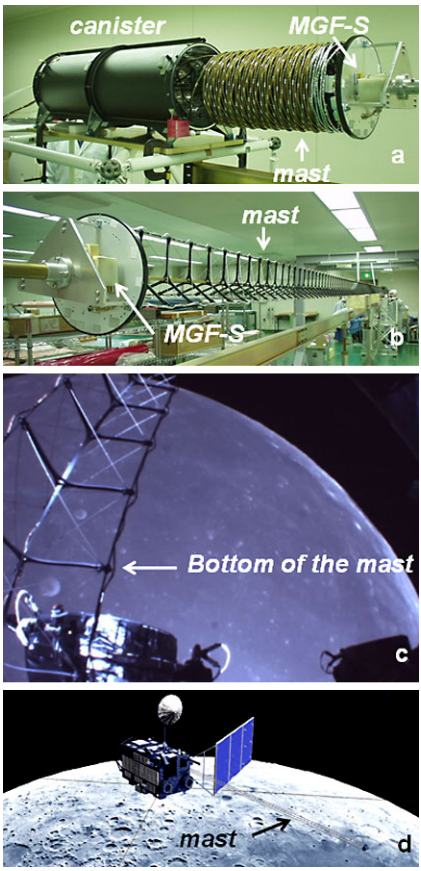

Fig. 1 Photographs of the deployment of the lunar magnetometer (LMAG) mast in the ground test (**a** and **b**), bottom part of the extended mast at 100 km altitude around the Moon by a monitor camera (**c**) and an image of LMAG onboard Kaguya (**d**). MGF-S, magnetometer of a triaxial ring-core sensor installed in a white box; canister, cylinder case (0.3 m in diameter and 0.9 m in length) for stowing the mast and installing the sensor alignment monitor coil (SAM-C) system. MGF-S is covered with multilayer insulation (MLI) when LMAG is mounted on Kaguya

to November, 2007 (Takahashi et al. 2009). Euler's rotation angles of the sensor alignment were almost the same on the dayside and nightside of the Moon within $\pm 0.1°$, and thus the mast was not significantly deformed due to temperature change in orbit. The sensor alignment was repeatedly assessed during the constancy phase since December 2007, resulting in good stability within $\pm 1.1°$. The zero offsets were determined with a modified version of the Davis-Smith method (Takahashi et al. 2009), to be almost stable within ± 0.3 nT during the constancy phase.

Subtracting the offsets, applying the Euler's rotation angles, and subsequently multiplying matrices for the coordinate transformation, we finally obtained the calibrated magnetic field in systems, such as GSE (Geocentric Solar Ecliptic), SSE (Selenocentric Solar Ecliptic) and ME (Mean Earth/Polar Axis) coordinates.

In order to check validity of the calibrations, a time series of the magnetic field observed by LMAG is compared with that of Advanced Composition Explorer spacecraft (ACE) at the Lagrange point 1. An example of the interplanetary magnetic field measurement on March 8, 2008 is shown in Fig. 2, when Kaguya periodically passed through the dayside and nightside of the Moon in the solar wind region. Taking into account a roughly one-hour delay due to the distance between the two spacecraft, the data show a good agreement in each component. It is also seen in Fig. 2 that the magnetic field measured by LMAG is partly altered from

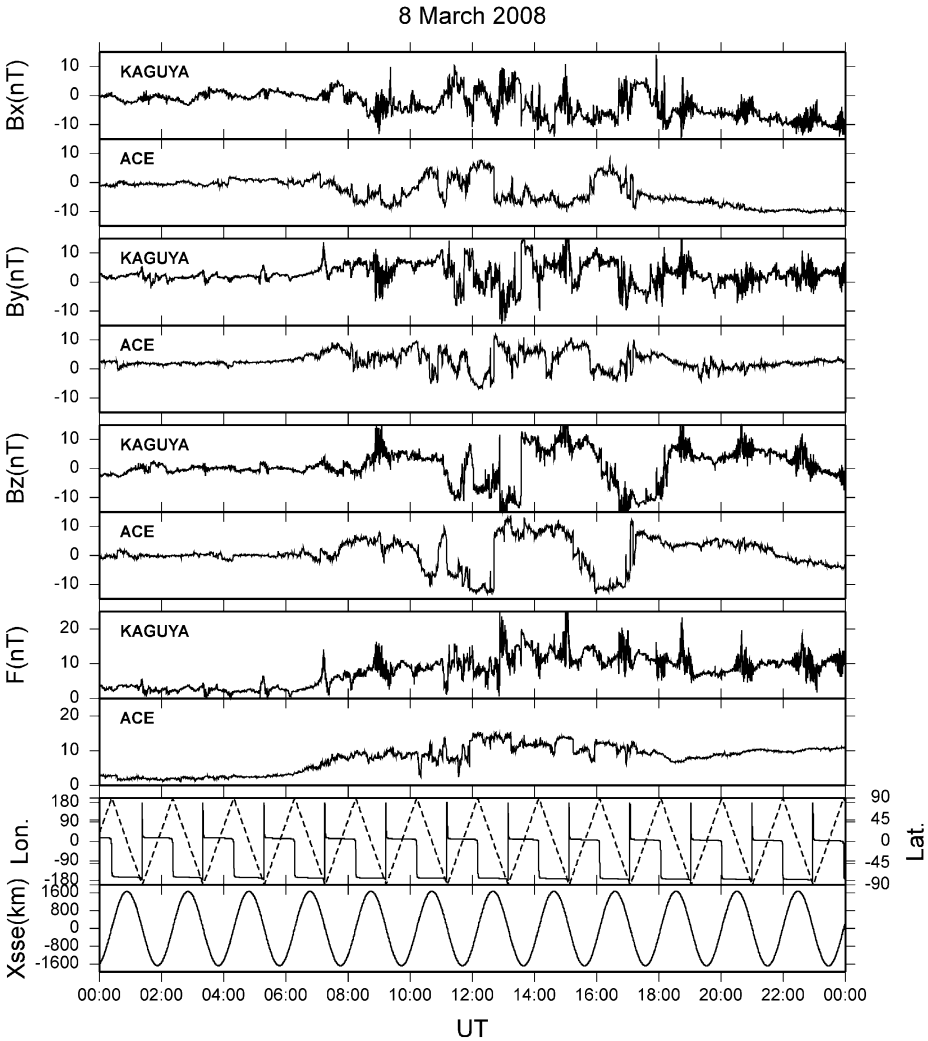

Fig. 2 The magnetic field data around the Moon observed by MAP-LMAG of Kaguya on March 8, 2008 are compared with the Advanced Composition Explorer (ACE) data at the Lagrange point 1. The Kaguya and ACE data are presented as mean values averaged for 1 second and 16 seconds, respectively, in the GSE coordinates (B_x, B_y, B_z and F). The horizontal axis is the universal time. Kaguya's mean position was at ($56R_E$, $10R_E$, $3R_E$) in the GSE coordinates where R_E is the Earth's radius. *In the bottom diagram*, Kaguya's positions are also shown in the selenographic (ME) latitude (*dashed line*) and longitude (*solid line*) and in the X_{SSE} of the Selenocentric Solar Ecliptic (SSE) coordinates. Taking into account a roughly 1-hour delay due to the distance of Kaguya from ACE, the magnetic field data of Kaguya are consistent with the ACE data. It is also seen that Kaguya repeatedly observed magnetic amplifications caused by the solar wind interactions at the terminator and above the lunar magnetic anomaly

that of ACE due to magnetic amplification at the terminator (e.g. Halekas et al. 2005) and magnetic enhancement above the lunar magnetic anomaly in the solar wind (Halekas et al. 2006). Therefore it is confirmed that the ground and in-orbit calibrations of LMAG were well determined.

3 Method of Mapping Magnetic Anomalies

When mapping the lunar magnetic anomaly, it is necessary to estimate the external field and to remove it from the calibrated magnetic field. It is not easy to distinguish crustal magnetic fields from external field changes of short wavelengths, since anomaly field intensities observed at ∼100 km altitude by LMAG are expected to be a few nano-tesla or less.

There have been some techniques of anomaly extraction by assuming low-degree polynomial functions of temporal change in the external field during a half of the orbiter revolution and by evaluating a cross correlation among orbit passes (e.g. Hood et al. 1981; Langel 1995; Purucker 2008). The low-degree polynomial approximation to the external field change is useful when a ratio of the anomaly-field intensity to the external field is not small, for example, in the tail lobe and at low altitudes. However, the external field around the Moon in the solar wind region is frequently disturbed even in the lunar wake. As shown later (Sect. 3.3), a lower bound of the representative period of external field changes is about 500 sec, that is, ∼800 km along track. Low-degree polynomial fitting cannot follow such components. At any rate, the track length in the lunar wake is often somewhat shorter than a half of the orbiter revolution, resulting in a shortage of polar region data and a possible bias due to a certain strong magnetic anomaly. Thus we have developed another de-trending technique applicable to a dataset of multiple orbits during one or more days in the tail lobe and the solar wind region. This technique also has an advantage that a possible magnetic anomaly in the polar region can be detected along a continuous track in contrast to the pole-to-pole pass analysis.

3.1 De-trending Data in the Tail Lobe

Applying the Bayesian statistical procedure (e.g. Tsunakawa 1992) to each component of multiple-orbit dataset, the observed magnetic field ($\boldsymbol{B}_{obs}$) is decomposed into the smooth trend of the external field ($\boldsymbol{B}_{trend}$) and the other component of relatively short periods ($\boldsymbol{B}_{short}$),

$$\boldsymbol{B}_{obs} = \boldsymbol{B}_{trend} + \boldsymbol{B}_{short}. \tag{3.1}$$

The trend is approximated with quadratic normalized B-spline functions s_j $(j = 1, \ldots, m)$ which are defined in time axis with $(m - 1)$ knots at equal intervals (see Appendix A by Tsunakawa 1992). $B_{trend,\alpha}$ ($\alpha = x, y, z$ in the Cartesian coordinates) is expressed in terms of

$$B_{trend,\alpha}(t_i) = \sum_{j=1}^{m} a_{\alpha,j} s_j(t_i), \tag{3.2}$$

where t_i is a time of ith observation $(i = 1, \ldots, n)$, and $a_{\alpha,1}, \ldots, a_{\alpha,m}$ are coefficients of the spline function. Usually we adopt $m = n$. This spline regression is to estimate a reasonable parameter of $\boldsymbol{a}_\alpha = (a_{\alpha,1}, \ldots, a_{\alpha,m})^t$, where superscript t denotes the transpose. Suppose that $B_{short,\alpha}(t_i)$ is independently subjected to a normal distribution with a zero mean and a variance of σ_α^2, $N(0, \sigma_\alpha^2)$, the likelihood function of $\boldsymbol{a}$ and σ_α^2 is

$$\begin{aligned} L(\boldsymbol{a}_\alpha, \sigma_\alpha^2) &= \prod_{i=1}^{n} \frac{1}{\sqrt{2\pi\sigma_\alpha^2}} \exp\left[-\frac{1}{2\sigma_\alpha^2}\{B_{obs,\alpha}(t_i) - B_{trend,\alpha}(t_i)\}^2\right] \\ &= \prod_{i=1}^{n} \frac{1}{\sqrt{2\pi\sigma_\alpha^2}} \exp\left[-\frac{1}{2\sigma_\alpha^2}\left\{B_{obs,\alpha}(t_i) - \sum_{j=1}^{m} a_{\alpha,j} s_j(t_i)\right\}^2\right] \end{aligned}$$

$$= \left(\frac{1}{2\pi\sigma_\alpha^2}\right)^{\frac{n}{2}} \exp\left[-\frac{1}{2\sigma_\alpha^2}\sum_{i=1}^{n}\left\{B_{obs,\alpha}(t_i) - \sum_{j=1}^{m} a_{\alpha,j}s_j(t_i)\right\}^2\right]. \tag{3.3}$$

Smoothness of the trend is considered here. The smoothest curve requires

$$\frac{d^2 B_{trend,\alpha}(t)}{dt^2} = 0, \tag{3.4}$$

for arbitrary time, and thus the trend is constituted by a straight line. If the second derivative is largely deviated from zero, the smoothness is lesser. Since the second derivative is equivalent to the second difference of $\boldsymbol{a}_\alpha$,

$$\Delta^2 a_{\alpha,j} \equiv a_{\alpha,j} - 2a_{\alpha,j-1} + a_{\alpha,j-2} \quad (j = 1, \ldots, m), \tag{3.5}$$

a Bayes model is constructed in association with a prior distribution of $\boldsymbol{a}_\alpha$, $\pi(\boldsymbol{a}_\alpha)$. Treatment of $a_{\alpha,0}$ and $a_{\alpha,-1}$ is referred to Tsunakawa (1992).

It is reasonably supposed that $\Delta^2 a_{\alpha,j}$ $(j = 1, \ldots, m)$ is independently subjected to a normal distribution with a zero mean and a variance of σ_Δ^2, $N(0, \sigma_\Delta^2)$. If

$$\sigma_\Delta^2 = u_\alpha^2 \sigma_\alpha^2, \tag{3.6}$$

the prior distribution is written below,

$$\pi(\boldsymbol{a}_\alpha|u_\alpha^2) = \prod_{j=1}^{m}\sqrt{\frac{u_\alpha^2}{2\pi\sigma_\alpha^2}} \exp\left[-\frac{u_\alpha^2}{2\sigma_\alpha^2}|\Delta^2 a_{\alpha,j}|^2\right] = \left(\frac{u_\alpha^2}{2\pi\sigma_\alpha^2}\right)^{\frac{m}{2}} \exp\left[-\frac{u_\alpha^2}{2\sigma_\alpha^2}\sum_{j=1}^{m}|\Delta^2 a_{\alpha,j}|^2\right]. \tag{3.7}$$

In this formula, u_α^2 is called the hyperparameter. Posterior distribution of $\boldsymbol{a}_\alpha$, $\pi_{post}(\boldsymbol{a}_\alpha|u_\alpha^2)$, is given from the Bayes theorem as

$$\pi_{post}(\boldsymbol{a}_\alpha|u_\alpha^2) \propto L(\boldsymbol{a}_\alpha, \sigma^2)\pi(\boldsymbol{a}_\alpha|u_\alpha^2) = \left(\frac{1}{2\pi\sigma_\alpha^2}\right)^{\frac{n}{2}} \left(\frac{u_\alpha^2}{2\pi\sigma_\alpha^2}\right)^{\frac{m}{2}} \exp\left[-\frac{S_\alpha}{2\sigma_\alpha^2}\right], \tag{3.8}$$

where

$$S_\alpha = \sum_{i=1}^{n}\left\{B_{obs,\alpha}(t_i) - \sum_{j=1}^{m} a_{\alpha,j}s_j(t_i)\right\}^2 + u_\alpha^2 \sum_{j=1}^{m}|\Delta^2 a_{\alpha,j}|^2. \tag{3.9}$$

Equation (3.9) indicates that u_α^2 corresponds to a tradeoff parameter between fidelity to the data (the first term on the right) and smoothness of the trend (the second term). Once u_α^2 is given, other parameters are automatically determined by minimizing S_α. Using matrices, (3.9) can be expressed as

$$S_\alpha = |\boldsymbol{b}_\alpha - X_\alpha \boldsymbol{a}_\alpha|^2, \tag{3.10}$$

where $\boldsymbol{b}_\alpha$ is an $(n+m)$ dimensional vector, $(B_{obs,\alpha}(t_1), \ldots, B_{obs,\alpha}(t_n), 0, \ldots, 0)^t$, and X_α is an $(n+m) \times m$ dimensional matrix (see Appendix B by Tsunakawa (1992)). u_α^2 is objectively determined by minimizing a log marginal likelihood, Akaike's Bayesian Information Criterion (ABIC; Akaike 1980),

$$\text{ABIC} = -2\ln\int \pi_{post}(\boldsymbol{a}_\alpha|u_\alpha^2)d\boldsymbol{a}_\alpha = n\ln\sigma_\alpha^{*2} + \ln(\det X_\alpha^t X_\alpha) - m\ln u_\alpha^2 + \text{const.}, \tag{3.11}$$

where $\sigma_\alpha^{*2} = S_\alpha/n$. In a practical way, we search a minimum ABIC and an optimal solution by giving $u_\alpha^2 = 2^k$, to say, $k = -5, \ldots, 20$, solving (3.10) and calculating ABIC from (3.11).

Since the above method does not require equal interval data, it is applicable to the dataset including some shortage of the observation (Tsunakawa 1992). Anomaly fields are estimated by interpolating the smooth trend at the observation time within the analyzed span and subtracting it from the observed field.

It is worth noting that the trend estimated from the tail lobe dataset is suited for the induction analysis of a possible metallic core since the lunar magnetic anomaly fields are removed. This application will be discussed elsewhere (Shimizu et al., in preparation).

3.2 De-trending Data in the Solar Wind Region

Equation (3.3) assumes that $\boldsymbol{B}_{short}$ is subjected to a single normal distribution and thus applicable to the dataset in the tail lobe. However, the fluctuation of the external field is different between dayside and nightside (the lunar wake as a strict definition) in the solar wind region. Thus we assume two kinds of tradeoff parameters in the solar wind region, $u_{\alpha,day}^2$ on dayside and $u_{\alpha,night}^2$ on nightside,

$$u_\alpha^2 = \begin{cases} u_{\alpha,night}^2 & \text{for } X_{\mathrm{SSE}} < 0 \text{ and } YZ_{\mathrm{SSE}} \equiv (Y_{\mathrm{SSE}}^2 + Z_{\mathrm{SSE}}^2)^{1/2} < R_L, \\ u_{\alpha,day}^2 & \text{for other cases,} \end{cases} \tag{3.12}$$

where suffix SSE denotes the SSE coordinates, and R_L is the Moon's radius.

Using two tradeoff parameters of dayside and nightside, posterior distribution is

$$\pi_{post}(\boldsymbol{a}_\alpha | u_\alpha^2) \propto \left(\frac{1}{2\pi\sigma_\alpha^2}\right)^{\frac{n}{2}} \left(\frac{u_{\alpha,day}^2}{2\pi\sigma_\alpha^2}\right)^{\frac{m_{day}}{2}} \left(\frac{u_{\alpha,night}^2}{2\pi\sigma_\alpha^2}\right)^{\frac{m_{night}}{2}} \exp\left[-\frac{S_\alpha}{2\sigma_\alpha^2}\right], \tag{3.13}$$

where m_{day} and m_{night} are the number of knots on dayside and nightside, respectively, and

$$S_\alpha = \sum_{i=1}^{n} \left\{ B_{obs,\alpha}(t_i) - \sum_{j=1}^{m} a_{\alpha,j} s_j(t_i) \right\}^2 + u_{\alpha,day}^2 \sum_{j_{day}=1}^{m_{day}} |\Delta^2 a_{\alpha,j_{day}}|^2 + u_{\alpha,night}^2 \sum_{j_{night}=1}^{m_{night}} |\Delta^2 a_{\alpha,j_{night}}|^2. \tag{3.14}$$

Thus,

$$\mathrm{ABIC} = n \ln \sigma_\alpha^{*2} + \ln(\det X_\alpha^t X_\alpha) - m_{day} \ln u_{\alpha,day}^2 - m_{night} \ln u_{\alpha,night}^2 + \mathrm{const.} \tag{3.15}$$

Using (3.14) and (3.15), we can objectively determine two tradeoff parameters to minimize ABIC and obtain an optimal solution in the similar way to the tail lobe dataset.

3.3 Re-sampling, Data Selection and Global Mapping

In global mapping, we used the data observed in the lunar wake and in the tail lobe, while the data of the dayside in the solar wind region were discarded. The external field trend is estimated from a dataset re-sampled from one-second time series, interpolated and subtracted from the original dataset to calculate tentative anomaly values at one-second intervals. The dataset expressed in the Cartesian coordinates is preferable in the present analysis, since the short-period component ($\boldsymbol{B}_{short}$) due to the external field change in the spherical coordinates fixed in the Moon is transformed and apparently variable along the orbit. As mentioned

in Sect. 3.2, we assume a normal distribution of $\boldsymbol{B}_{short}$. If a strong magnetic anomaly is observed in a calm external field, the anomaly field seems not to be subjected to a normal distribution along a single pole-to-pole pass. However, we simultaneously analyze data along about 12 orbits shifting westward successively during a one-day observation and thus possibly avoid an ill-posed problem.

In the present analysis, the Bayesian statistical procedure is applied to the data re-sampled at 90-second intervals from a one-day dataset of about 12 orbits. This re-sampling rate has a Nyquist frequency of 1/180 Hz, which assumes that external fields are described mainly by lower frequencies than 1/180 Hz. From the spectral analysis of the magnetic field around the Moon, frequencies lower than 1/100 Hz dominate in the solar wind region (e.g. Nakagawa et al. 2010). We show examples of the dynamic spectra of the magnetic field in the solar wind and tail lobe regions (Figs. 3 and 4). It is seen that dominant frequencies are

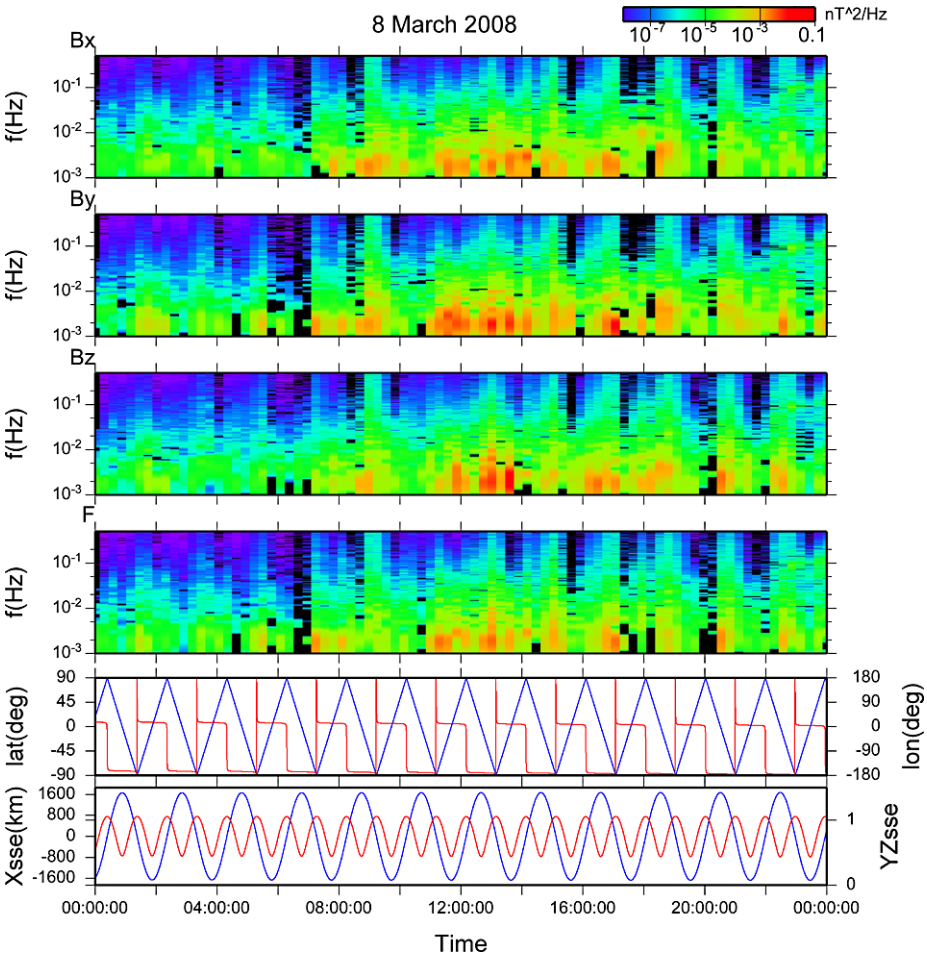

Fig. 3 Dynamic spectra of three components and total force of the magnetic field in the solar wind region (March 8, 2008) as in Fig. 2. Fourier transformation was applied to each of 1024 second sections. B_x, B_y, B_z, X_{SSE} (*blue line*) and $YZ_{\mathrm{SSE}} \equiv \sqrt{Y_{\mathrm{SSE}}^2 + Z_{\mathrm{SSE}}^2}/R_L$ (R_L, the Moon's radius; *red line*) are in the SSE coordinates, while the latitude (*blue line*) and the longitude (*red line*) are in the ME coordinates

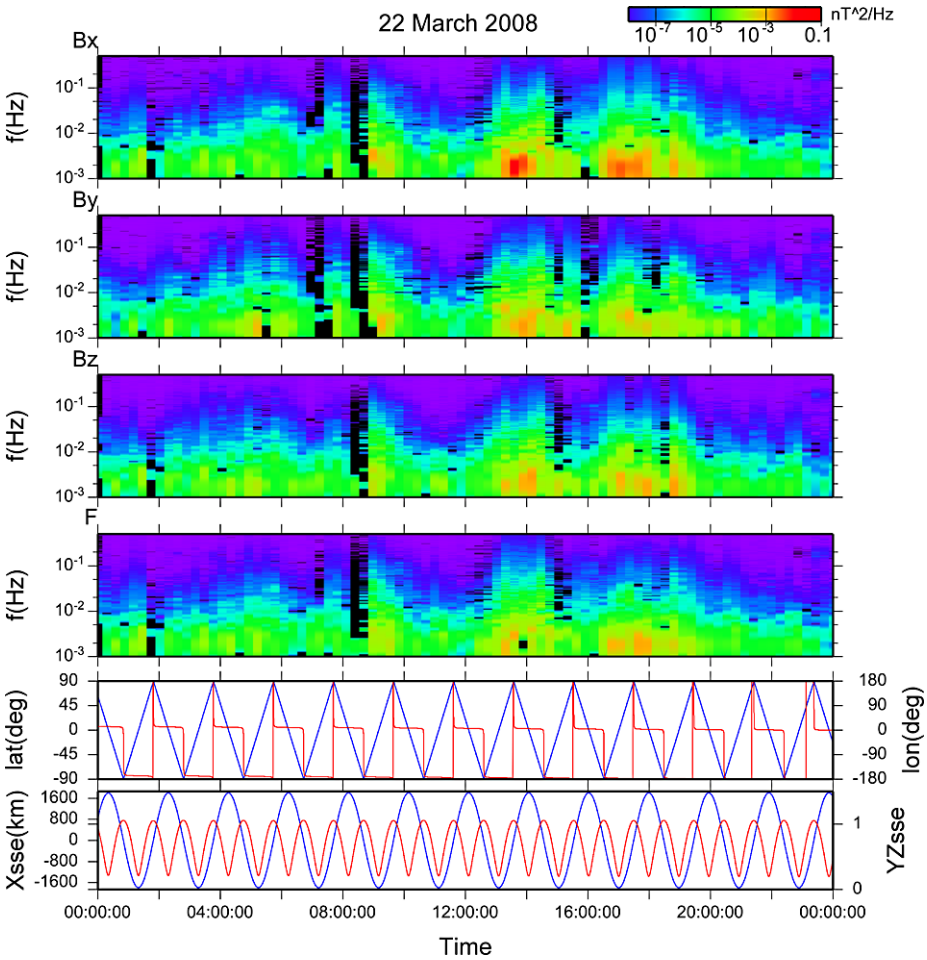

Fig. 4 Dynamic spectra of three components and total force of the magnetic field in the tail lobe region (March 22, 2008). Kaguya's mean position was at $(-61R_E, -9R_E, 4R_E)$ in the GSE coordinates. Symbols are the same in Fig. 3. It is noted that Kaguya was in the plasma sheet around 10:00, 14:00 and 18:00

lower than 1/100 Hz, in particular, lower than ∼1/500 Hz (wavelength of ∼800 km along track) on the nightside of the solar wind region and in the tail lobe region. Thus the trend of the external field can be described when the re-sampling rate is at 90-second intervals. According to the spherical harmonic analysis of the lunar magnetic anomaly (Purucker 2008), its distribution is presented mainly by the spherical harmonics of higher degrees than ∼15. This suggests that the typical wavelength of the lunar magnetic anomaly is shorter than ∼700 km. Thus our re-sampling rate is reasonable, although the frequency ranges are not clearly separated between the external field change and the magnetic anomaly field along the track.

If the tentative anomalies of each pass show a relatively small standard deviation of the tentative anomaly field (r.m.s. of $B \leq 1.5$ nT) and a relatively slow change (r.m.s. of $dB/dt \leq 0.2$ nT/sec), the dataset is used in further analysis. Otherwise, the dataset is discarded to avoid severe effects of the external field fluctuation. The former criterion means

that a pass with frequent appearance of an anomaly field larger than 3 nT, twice the r.m.s. of B, is rejected. This threshold is estimated from the Apollo mission results (e.g. Dyal et al. 1974) and a case study of the Reiner Gamma magnetic anomaly (Kurata et al. 2005), which is one of the strongest anomalies. Their dipole source model of the Reiner Gamma anomaly suggests that the anomaly field is less than ∼3 nT at 100 km altitude. The latter criterion gives a constraint on high-frequency components based on the instrumental noise level (see Sect. 2.1). Assuming a sinusoidal change of the magnetic field with a peak-to-zero amplitude of 0.05 nT and a Nyquist frequency of the one-second dataset (1/2 Hz), its r.m.s. of dB/dt is ∼0.11 nT/sec. For safety, a value of 0.2 nT/sec is taken as a threshold in the present study.

The selected data of three components and the calculated total forces are put into a $1^\circ \times 1^\circ$ bin in the ME coordinate system. Within a bin, excluding data out of three standard deviations to avoid an effect of occasionally anomalous values, a mean value and a standard deviation are recalculated. If a bin includes less than fifteen data, it is regarded as insufficient and counted as vacant.

3.4 Altitude Normalization

Satellite observations of the magnetic anomaly field are performed at more or less different altitudes due to the orbit configuration. If the altitude variation is not large, the original dataset can be used in global mapping. Otherwise, it is necessary that measured anomaly fields are normalized to a certain constant altitude. Recently some techniques of the normalization have been applied to the LP data in mapping the lunar magnetic anomaly.

An empirical power law is applied to the upward and downward continuations in calculating anomaly amplitudes at 30 and 40 km altitudes in the preliminary global mapping of LP (Richmond and Hood 2008). This law assumes that the magnitude of the anomaly field is subjected to a power law empirically determined by a ratio between the observed and normalized altitudes. Although this power law may be useful for projecting the magnetic field data onto a spherical plane at a constant altitude close to the observation points, its theoretical background has not been given.

The equivalent source model using surface dipoles was applied to global mapping of the lunar magnetic anomaly (Purucker 2008). In this model, the lunar crust is divided into blocks, each on which is assumed to have a horizontal magnetic dipole fixed at its center of the surface. Magnetic potential is deduced from the dipoles, and anomaly fields are calculated at arbitrary altitudes. Thus the dipoles can be determined as an inverse problem of two components of dipoles to fit the magnetic field observation. However, the magnitude and direction of dipoles are not physically interpreted since they are simply tools in the analysis (Purucker 2008).

Another equivalent source model using magnetic charges on the surface, the Equivalent Pole Reduction (EPR) method, was applied to the Reiner Gamma anomaly using the LP dataset (Toyoshima et al. 2008). In this method, the lunar surface is divided into blocks with positive or negative magnetic charges (surface magnetic poles) like electric charges, and then magnetic fields are calculated at arbitrary altitudes. Thus the EPR method is regarded as an inverse problem of a surface density distribution of equivalent poles to fit the magnetic field observation. Compared with the equivalent dipole model by Purucker (2008), the inversion of the EPR method is more easily solved, since the surface density of equivalent poles is scalar. Physical meaning of the equivalent pole distribution is discussed and clarified later.

It is well known that magnetic sources cannot uniquely be determined from the magnetic field observation. Also, it is mathematically proven that the static magnetic field at any position outside internal sources (or inside external sources) is determined from a distribution of

specific scalar values on the boundary plane. This is called the boundary value problem, and there are three possible boundary values corresponding to the first boundary value problem (Dirichlet problem), the second boundary value problem (Neumann problem) and the third boundary value problem (Cauchy problem). Thus the altitude normalization of the satellite data can be performed by solving an inverse boundary value problem and calculating the magnetic field at a certain constant altitude. In this subsection we briefly review principle of the boundary value problem and clarify physical meaning of equivalent poles on the surface. Based on the inverse boundary value problem, we show the altitude normalization, in particular, the EPR method.

3.4.1 Principle of the Boundary Value Problem

The boundary value problem in the spherical coordinates (r, θ, φ) is briefly reviewed in the following (e.g. Roach 1982; Jackson 1998). Assuming a boundary of $r = R$ and magnetic sources of $r < R$, magnetic potential $\psi(\boldsymbol{r})$ at a point of vector $\boldsymbol{r}(r, \theta, \varphi; x, y, z)$ in space of $r > R$ is expressed as,

$$\psi(\boldsymbol{r}) = R \sum_{n=1}^{\infty} \left(\frac{R}{r}\right)^{n+1} Y_n(\theta, \varphi), \tag{3.16}$$

$$Y_n(\theta, \varphi) = \sum_{m=0}^{n} (G_n^m \cos m\varphi + H_n^m \sin m\varphi) P_n^m(\cos\theta), \tag{3.17}$$

where Y_n is an n-degree spherical harmonic function, P_n^m is a non-normalized-associated Legendre function of n-degree and m-order, and G_n^m and H_n^m are spherical harmonic coefficients.

It is known that boundary value $U(\theta_s, \varphi_s)$ at a point of $\boldsymbol{r}_s(R, \theta_s, \varphi_s)$ is determined by the linear combination of $\psi(\boldsymbol{r}_s)$ and $\partial\psi/\partial r|_{\boldsymbol{r}_s}$,

$$U(\theta_s, \varphi_s) = a\psi(\boldsymbol{r}_s) + b \left.\frac{\partial \psi}{\partial r}\right|_{\boldsymbol{r}_s}, \tag{3.18}$$

where a and b are constant coefficients, and suffix S denotes the surface. This formulation corresponds to the Dirichlet problem for $a = 1$ and $b = 0$, the Neumann problem for $a = 0$ and $b = 1$, and the Cauchy problem for $a \neq 0$ and $b \neq 0$. It is noted that a ratio of a/b has a dimension of R^{-1} for the Cauchy problem.

Transforming the equations, we can obtain the relationship of the potential with the boundary value in terms of

$$\psi(\boldsymbol{r}) = \iint_S U(\theta_s, \varphi_s) K(r, \theta, \varphi; \theta_s, \varphi_s) dS, \tag{3.19}$$

$$K(r, \theta, \varphi; \theta_s, \varphi_s) = \frac{1}{4\pi R} \sum_{n=0}^{\infty} \left(\frac{R}{r}\right)^{n+1} \frac{2n+1}{aR - b(n+1)} P_n(\cos\Theta), \tag{3.20}$$

$$\cos\Theta = \cos\theta\cos\theta_s + \sin\theta\sin\theta_s\cos(\varphi - \varphi_s), \tag{3.21}$$

where $P_n(\cos\Theta) = P_n^0(\cos\Theta)$, and Θ is an angle between $\boldsymbol{r}$ and $\boldsymbol{r}_s$. Since a *zero*-degree term of $\psi(\boldsymbol{r}_s)$ should be null,

$$\iint_S U(\theta_s, \varphi_s) dS = 0. \tag{3.22}$$

This indicates that sum-of-boundary values on the surface should be zero. The magnetic field is given in terms of

$$\boldsymbol{B}(\boldsymbol{r}) = -\mu_0 \nabla \psi(\boldsymbol{r}) = -\mu_0 \int\int_S U(\theta_s, \varphi_s) \nabla K(r, \theta, \varphi; \theta_s, \varphi_s) dS, \tag{3.23}$$

where ∇ is a gradient operator with respect to $\boldsymbol{r}$.

Since the kernel $K(r, \theta, \varphi; \theta_s, \varphi_s)$ should be convergent, a and b are taken to be specific values. For $a = 1$ and $b = 0$ (Dirichlet problem), $U(\theta_s, \varphi_s) = \psi(\boldsymbol{r}_s)$, the kernel K is

$$K = \frac{1}{4\pi R} \sum_{n=0}^{\infty} (2n+1) \eta^{n+1} P_n(\xi), \tag{3.24}$$

where $\eta = R/r$ and $\xi = \cos\Theta$. In this case, the boundary value is a magnetic potential. According to the formula of the series of Legendre functions,

$$\sum_{n=0}^{\infty} (2n+1) \eta^n P_n(x) = \frac{1-\eta^2}{L^3}, \tag{3.25}$$

where $L = (1 - 2\eta\xi + \eta^2)^{1/2}$. Therefore, the kernel is convergent in an analytic form,

$$K = \frac{1}{4\pi R} \frac{\eta(1-\eta^2)}{L^3} = \frac{1}{4\pi R} \frac{\overline{r}^2 - 1}{\overline{r}'^3}, \qquad \nabla K = \frac{1}{4\pi R^2} \left\{ \frac{2\overline{\boldsymbol{r}}}{\overline{r}'^3} - \frac{3(\overline{\boldsymbol{r}}^2 - 1)(\overline{\boldsymbol{r}} - \overline{\boldsymbol{r}}_s)}{\overline{r}'^5} \right\}, \tag{3.26}$$

where $\overline{\boldsymbol{r}} = \boldsymbol{r}/R$ and $\overline{\boldsymbol{r}}' = (\boldsymbol{r} - \boldsymbol{r}_s)/R$.

For $a = 0$ and $b = 1$ (Neumann problem),

$$U(\theta_s, \varphi_s) = \left. \frac{\partial \psi}{\partial r} \right|_{\boldsymbol{r}_s} = -\frac{1}{\mu_0} B_r(\boldsymbol{r}_s), \tag{3.27}$$

$$\begin{aligned} K &= -\frac{1}{4\pi R} \sum_{n=0}^{\infty} \frac{2n+1}{n+1} \eta^{n+1} P_n(\xi) \\ &= -\frac{1}{4\pi R} \left\{ 2 \sum_{n=0}^{\infty} \eta^{n+1} P_n(\xi) - \sum_{n=0}^{\infty} \frac{1}{n+1} \eta^{n+1} P_n(\xi) \right\}. \end{aligned} \tag{3.28}$$

In this case, the boundary value is corresponding to a negative value of radial component of the surface magnetic field. In other words, the magnetic field above the surface is determined by the poloidal field while the toroidal field is confined to the surface. According to the formulae,

$$\sum_{n=0}^{\infty} \eta^{n+1} P_n(x) = \frac{\eta}{L}, \tag{3.29}$$

and

$$\sum_{n=0}^{\infty} \frac{1}{n+1} \eta^{n+1} P_n(\xi) = \ln\left(1 + \frac{2\eta}{1 - \eta + L}\right). \tag{3.30}$$

Therefore the kernel is convergent,

$$\begin{aligned} K &= -\frac{1}{4\pi R}\left\{\frac{2\eta}{L} - \ln\left(1 + \frac{2\eta}{1-\eta+L}\right)\right\} = -\frac{1}{4\pi R}\left\{\frac{2}{\overline{r}'} - \ln\left(1 + \frac{2}{\overline{r}+\overline{r}'-1}\right)\right\}, \\ \nabla K &= \frac{1}{2\pi R^2}\left\{\frac{\overline{\boldsymbol{r}}-\overline{\boldsymbol{r}}_s}{\overline{r}'^3} - \frac{1}{(\overline{r}+\overline{r}'+1)(\overline{r}+\overline{r}'-1)}\left(\frac{\overline{\boldsymbol{r}}}{\overline{r}} + \frac{\overline{\boldsymbol{r}}-\overline{\boldsymbol{r}}_s}{\overline{r}'}\right)\right\}. \end{aligned} \tag{3.31}$$

For $a = -1/R$ and $b = -2$ (one of the Cauchy problems), the kernel is convergent,

$$U(\theta_s, \varphi_s) = -\frac{1}{R}\psi(\boldsymbol{r}_s) + \frac{2}{\mu_0}B_r(\boldsymbol{r}_s), \tag{3.32}$$

$$K = \frac{1}{4\pi R}\sum_{n=0}^{\infty}\eta^{n+1}P_n(x) = \frac{1}{4\pi R}\frac{\eta}{L} = \frac{1}{4\pi R}\frac{1}{\overline{r}'}. \tag{3.33}$$

Therefore,

$$\nabla K = -\frac{1}{4\pi R^2}\frac{\overline{\boldsymbol{r}}-\overline{\boldsymbol{r}}_s}{\overline{r}'^3} = -\frac{\boldsymbol{r}-\boldsymbol{r}_s}{4\pi r'^3}, \tag{3.34}$$

$$\boldsymbol{B}(\boldsymbol{r}) = \int\int_S \frac{\mu_0 U(\theta_s, \varphi_s)}{4\pi}\frac{\boldsymbol{r}-\boldsymbol{r}_s}{r'^3}dS. \tag{3.35}$$

Equation (3.35) indicates that $\mu_0 U(\theta_s, \varphi_s)$ for $a = -1/R$ and $b = -2$ corresponds to surface magnetic charges, that is, equivalent poles. In other words, the equivalent pole is a mixture of the potential $\psi(\boldsymbol{r}_s)$ and the radial component of the surface magnetic field $B_r(\boldsymbol{r}_s)$. From (3.28), the term of the Neumann-type kernel for $n \geq 4$ is dominated by the first term on the right side. Compared with (3.33), the equivalent pole distribution can yield a good approximation of $2B_r(\boldsymbol{r}_s)$ for $n \geq 4$, that is, a wavelength shorter than ~2600 km on the lunar surface.

3.4.2 Altitude Normalization Based on the Inverse Boundary Value Problem

If boundary values are given, the magnetic field at an arbitrary position outside magnetic sources can be calculated. As an inverse problem, boundary values are obtained from magnetic field data observed at different positions. Thus the observation dataset can be normalized to a constant altitude via boundary values, and the magnetic field can be interpolated if there is a shortage of observation.

We take the lunar surface as a boundary, hereafter. Dividing the surface into M bins, the magnetic field is approximated by boundary values at the center of bins,

$$\boldsymbol{B}(\boldsymbol{r}) \approx -\mu_0\sum_{j=1}^{M}U(\theta_j, \varphi_j)\nabla K(r, \theta, \varphi; \theta_{s,j}, \varphi_{s,j})S_j, \tag{3.36}$$

where $(\theta_{s,j}, \varphi_{s,j})$ and S_j are a center position and an area of jth bin, respectively. The magnetic field at an altitude of h is affected mainly by boundary values within a circle of radius h beneath the observation point. Thus we should take a size smaller than h for each bin.

When the magnetic field is observed at $\boldsymbol{r}_i$ $(i = 1, \ldots, N)$,

$$\begin{bmatrix} \boldsymbol{B}(\boldsymbol{r}_1) \\ \vdots \\ \boldsymbol{B}(\boldsymbol{r}_N) \end{bmatrix} = \begin{bmatrix} T_{1x,1} & \cdots & T_{1x,M} \\ \vdots & \ddots & \vdots \\ T_{Nz,1} & \cdots & T_{Nz,M} \end{bmatrix} \begin{bmatrix} U(\boldsymbol{r}_{s,1}) \\ \vdots \\ U(\boldsymbol{r}_{s,M}) \end{bmatrix}, \tag{3.37}$$

$$T_{i\alpha,j} = -\mu_0[\nabla_{\boldsymbol{r}} K(r_i, \theta_i, \varphi_i; \theta_{s,j}, \varphi_{s,j})]_\alpha S_j, \tag{3.38}$$

where $\boldsymbol{r}_i = (r_i, \theta_i, \varphi_i)$ and $\boldsymbol{r}_{s,j} = (R, \theta_{s,j}, \varphi_{s,j})$. Thus,

$$\begin{bmatrix} U(\boldsymbol{r}_{s,1}) \\ \vdots \\ U(\boldsymbol{r}_{s,M}) \end{bmatrix} = (T^t T)^{-1} T^t \begin{bmatrix} \boldsymbol{B}(\boldsymbol{r}_1) \\ \vdots \\ \boldsymbol{B}(\boldsymbol{r}_N) \end{bmatrix}, \tag{3.39}$$

where $T = (T_{i,j})$. An optimal solution of U is given by the least square fitting to the observed magnetic field.

Since (3.39) is considered to be deconvolution, the noise included in the observed magnetic field tends to be amplified and to disturb boundary values. Thus we consider smoothness of the boundary value distribution in a similar way to the de-trending technique in Sect. 3.1. Approximating that adjacent bins are on a plane, we take a second difference of U as the representative smoothness as

$$\Delta U_j \approx 4U_j - (U_{j,1} + U_{j,2} + U_{j,3} + U_{j,4}), \tag{3.40}$$

where U_j is a boundary value of jth bin, and $U_{j,k}$ $(k = 1, \ldots, 4)$ are boundary values of its surrounding bins. If $\Delta U_j = 0$, distribution of boundary values is smoothest. Assuming that ΔU_j is subjected to a zero-mean normal distribution, prior and posterior distributions and ABIC are defined (Toyoshima et al. 2008). Minimizing ABIC, we obtain the most likely distribution of boundary values.

In the present study, the EPR method improved for global mapping (Shibuya et al., in preparation) is applied to the dataset of the magnetic anomaly in $1^\circ \times 1^\circ$ bin format. Since the computer resource is limited, it is difficult to obtain an equivalent pole distribution of the whole lunar surface simultaneously. Thus the lunar surface is divided into ten regions: four middle-latitude regions of the northern hemisphere (0° to 60° N in latitude, and 305° E to 45° E, 45° E to 135° E, 135° E to 215° E and 215° E to 305° E in longitude; $0.5^\circ \times 0.5^\circ$ bin) and a north polar region (60° N to 90° N; $0.5^\circ \times 1^\circ$ bin), and also the same divisions in the southern hemisphere. Those regions overlap to some extent. We solve an inverse problem of each region and connect the equivalent pole distributions to cover the whole surface. It is noted that equivalent poles of overlapping bins show a good consistency between the adjacent regions within estimated error levels in the present analysis.

3.5 Subtraction of the External Field Changes and Random Noise

In the present anomaly analysis, we need a careful treatment of the data observed at high altitude since signatures of the crustal magnetic field is comparable to the external field change as mentioned before. In this subsection, we summarize the subtraction of the external field changes and noises to be the following three procedures.

(i) The Bayesian procedure of de-trending is effective especially for subtracting the external field changes of various longer wavelengths, since we assume only the smoothness

without analytical functions of time. Based on the spectral analyses of the observed magnetic fields, the re-sampling interval, 90 sec in the present study, is determined from a lower bound of main components of the usual external-field change. This re-sampling may work like a low-pass filter. A tradeoff parameter between the fidelity to the observed data and the smoothness of the external field trend is objectively determined using statistical information of ABIC.

(ii) The selection criteria of the pass are basically determined from the upper bound of the lunar magnetic field at ∼100 km altitude and from the instrumental noise. The former criterion may reject an occasionally anomalous field due to a step-like change of the external field such as a shock wave. The latter criterion like a high-cut filter may be effective for quantitatively and routinely distinguishing the pass in the magnetosheath and plasma sheet of the Earth.

(iii) Even after the above procedures, noise components possibly affect within-bin averaged values. The altitude normalization based on the inverse boundary value problem can further reduce noise effects by evaluating the static field due to the crustal magnetization like the cross correlation among the bin data.

4 Results of Mapping Magnetic Anomalies

4.1 De-trending Results

The method of mapping magnetic anomalies in Sect. 3 was applied to a time series of one-second average data which were observed at a nominal altitude of ∼100 km in a polar orbit during November 2007 to December 2008. About 20% of 14-month data passed the selection criteria. As a result, coverage of the initial global mapping in $1^\circ \times 1^\circ$ bins from the nominal observation is about 95% of the lunar surface. Since the solar activity has been very low during the observation, an effect of the external field fluctuation is small enough to detect a weak signal of the lunar magnetic anomalies at ∼100 km altitude.

One of the typical examples of magnetic anomaly fields after de-trending is shown as wiggle maps along orbit passes for the southeastern part of the farside (Fig. 5). The magnetic fields in Fig. 5 were observed along 185° E–222° E passes in the tail lobe (September 13–16, 2008) and 225° E–246° E passes on the nightside of the solar wind region (November 5–6, 2008). It is seen that each map of three components shows a good correlation between adjacent passes, although most of the anomaly amplitudes are less than 3 nT.

For example, Fig. 6 shows de-trending results along a 240° E pass by the Bayesian procedure in the Cartesian coordinates together with those by the quadratic polynomial fitting. The Bayesian results are part of a one-day analysis of about 12 orbits including both of the lunar nightside and dayside, while the quadratic polynomial fitting is applied to the pass in the wake. Most features of both methods are nearly identical within ∼0.1 nT. However, offset-like deviations of 0.1–0.2 nT along the pass are seen in the northern section of the quadratic polynomial fitting results. This long-wavelength deviation seems to be caused by an effect of a large anomaly field around 20° S (the Crisium antipode anomaly). On the other hand, such an offset-like deviation does not remain in the corresponding part of the Bayesian one-day analysis. Thus small signatures are more detectable in the present analysis.

4.2 Overview of Initial Global Mapping at 100 km Altitude

Initial global mapping results of the lunar magnetic anomaly without altitude correction are shown in Lambert equal area projections (Figs. 7 and 8). Altitudes during the observation

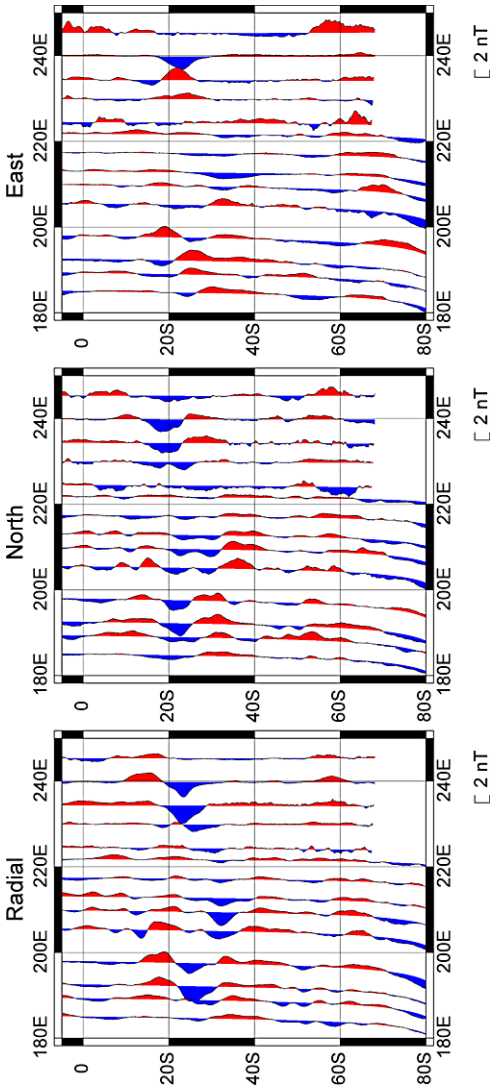

Fig. 5 Wiggle maps of radial, north and east components in the ME coordinates along the observation track over the southeastern region of the farside (positive, *red*; negative, *blue*)

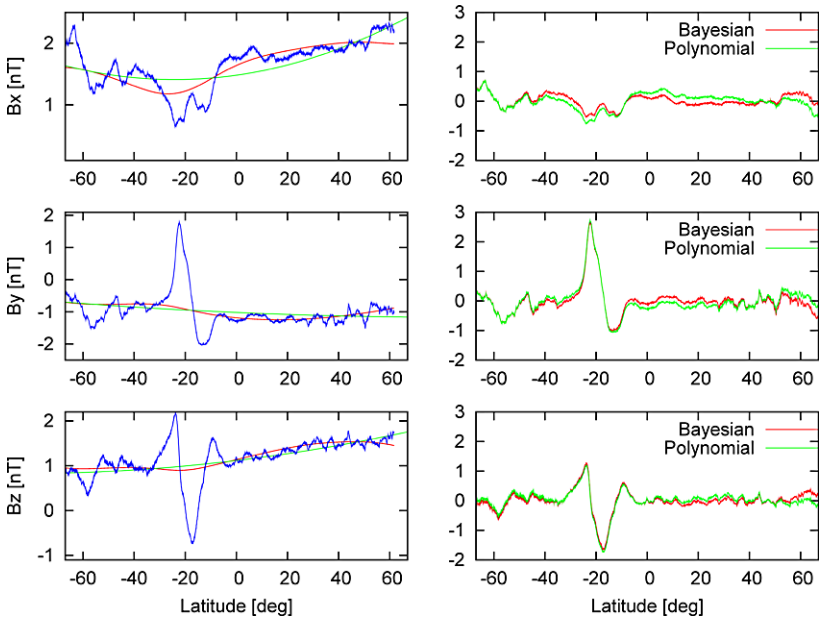

Fig. 6 De-trending results of three components by the Bayesian procedure in comparison with those by the quadratic polynomial fitting for the pass of 240° E in Fig. 5. *Blue line*, the observation before de-trending; *red line*, the result by the Bayesian procedure; *green line*, the result by the quadratic polynomial fitting. The Bayesian results are part of one-day analysis of about 12 orbits including both of the lunar nightside (wake) and dayside, while the quadratic polynomial fitting was applied to the pass of night side as shown by *blue lines*

period range from 70 to 130 km, mostly within 100 ± 10 km, and altitudes on the nearside tend to be slightly higher than on the farside (Fig. 7).

The observed anomaly field is regarded as a static field of the lunar crustal magnetization with random disturbances due to the external field fluctuation, the instrumental noise and the altitude fluctuation. Thus a standard error (se) is calculated as a representative error of the mean anomaly field at the mean altitude for each bin (Fig. 9). It is seen in Fig. 9 that about 99% of bins have errors of three components of $\leq$0.1 nT (1 se). Thus we can study the high-altitude anomaly field of less than 1 nT with sufficient precision.

Several strong anomalies are clearly seen on the map of total force in logarithmic scale (Fig. 7), although their intensities are less than 4 nT. Weak and north-south elongated anomalies in the total force map may be caused by an insufficient removal of the external field change and possibly disturb the identification of the crustal anomaly. In this case, the radial, north and east component maps are useful, since magnetic anomalies of crustal magnetization are identified as a pair of positive and negative fields and then distinguishable from noises (Fig. 8).

It is seen in Figs. 7 and 8 that an anomaly cluster is distributed at the northwestern edge of the South-Pole Aitken (SPA) basin on the farside and several isolated anomalies on both the nearside and farside. This overview of the anomaly distribution from the Kaguya observation at $\sim$100 km altitude is well consistent with previous works (e.g. Richmond and Hood 2008). Distinctly identified are anomalies in the Descartes crater region (DC), the Stöfler crater region (ST) and the Crisium basin region (CR) on the nearside, and in the Crisium antipode region (CA), the Serenitatis antipode region (SA) and the Imbrium antipode region (IA)

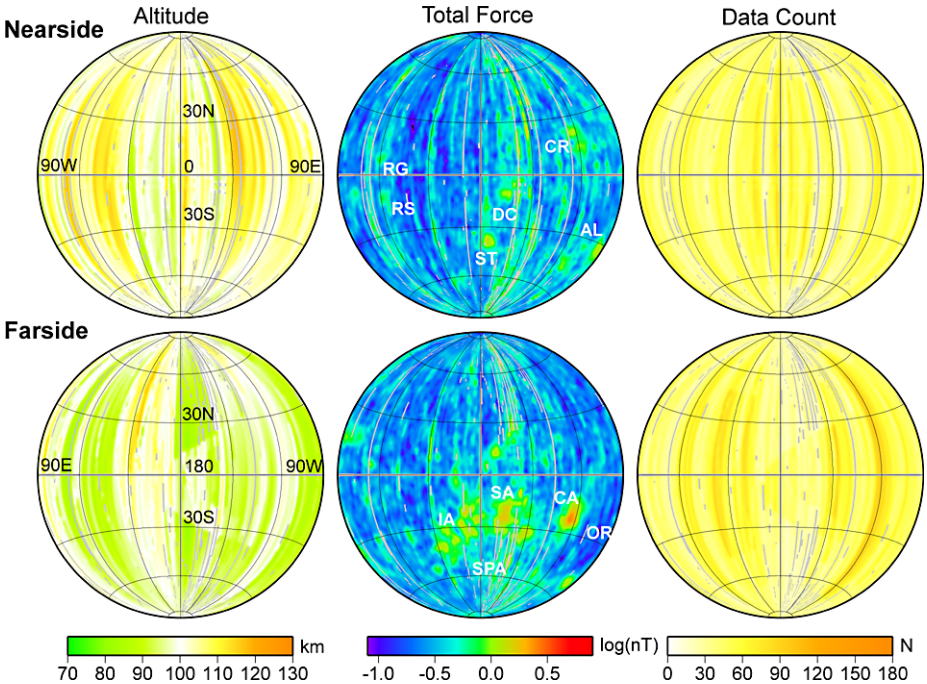

Fig. 7 Distributions of the altitude (*left*), the total force (*middle*) and the data counts of a 1° × 1° bin (*right*) during the constancy phase (∼100 km altitude) in Lambert equal area projection. *Gray color* indicates that the bin does not include sufficient data, that is, a vacant bin on the map. The data used in the mapping were selected from LMAG observations in the lunar wake and in the tail lobe regions (November 2007 to December 2008). The *color scale* of the total intensity is logarithmic. CR, Crisium basin; DC, Decartes crater; ST, Stöfler crater region; RS, Rima Sirsalis; IA, Imbrium antipode; SA, Serenitatis antipode; CA, Crisium antipode; OR, Orientale basin; AL, near Abel crater; SPA, South Pole-Aitken basin

on the farside. The strongest anomaly of ∼3 nT is located in the Crisium antipode region. Relatively weaker anomalies are recognized in the Reiner Gamma region (RG), the Rima Sirsalis region (RS) and the Abel crater region (AL) on the nearside. On the other hand, the Orientale basin (OR), which is considered the youngest on the Moon, shows no significant anomaly.

The anomaly field normalized to a constant altitude of 100 km by the EPR method is shown for three components in Fig. 10 and for total force in Fig. 11a. An error level is estimated to be ±0.20 nT for each component at 100 km altitude. Characteristic features of the relatively strong anomalies in the altitude-normalized maps are almost the same as those in the map without altitude correction, while noise-like components are reduced in Figs. 10 and 11a. As a result, it is easier to distinguish crustal anomalies in the total force map, although the anomalies are slightly smoothed. Using the altitude-normalized anomaly maps by Kaguya, we identify and describe magnetic anomalies in more detail, compared with the previous study of LP mapping at 30 km altitude (Richmond and Hood 2008, RH08 hereafter), in particular, concerning the anomaly locality on the total force maps in logarithmic scale (Figs. 11a and b). For the RH08 total force map, all of the anomaly field data at 30 km altitude provided by Richmond and Hood (2008) were put in 1° × 1° bins, and average values are mapped in Fig. 11b. Although Richmond and Hood (2008) do not explicitly map anomaly fields of intensities smaller than 3 nT in total force, such small anomalies are also

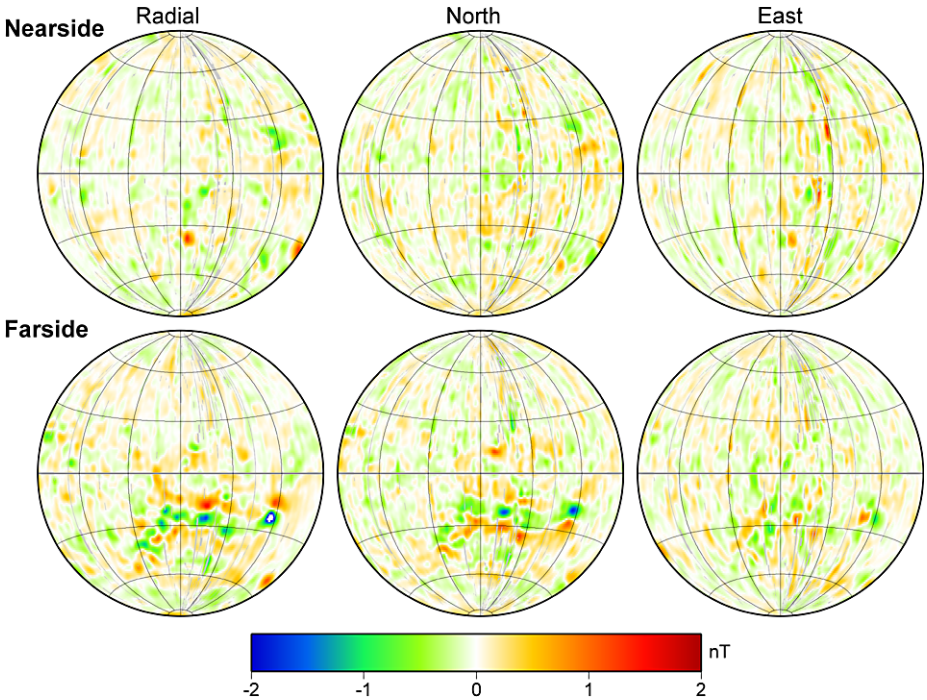

Fig. 8 Three components of the lunar magnetic anomaly from the Kaguya observations during the constancy phase are shown in the ME coordinates as in Fig. 7. The *color scale* is linear, and the *white area* in the Crisium antipode region on the farside denotes lower than −2 nT

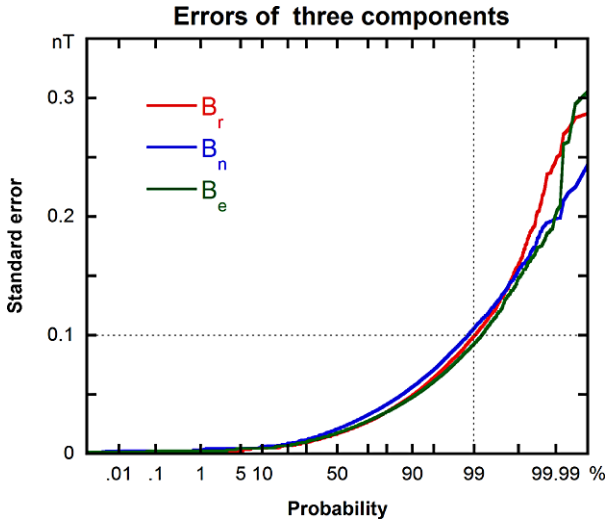

Fig. 9 Probability distribution of standard errors of three components (B_r, radial; B_n, north; B_e, east) in $1^\circ \times 1^\circ$ bin (Fig. 8). It is seen that 99% of bins show standard errors $\leq$0.1 nT (*broken lines*)

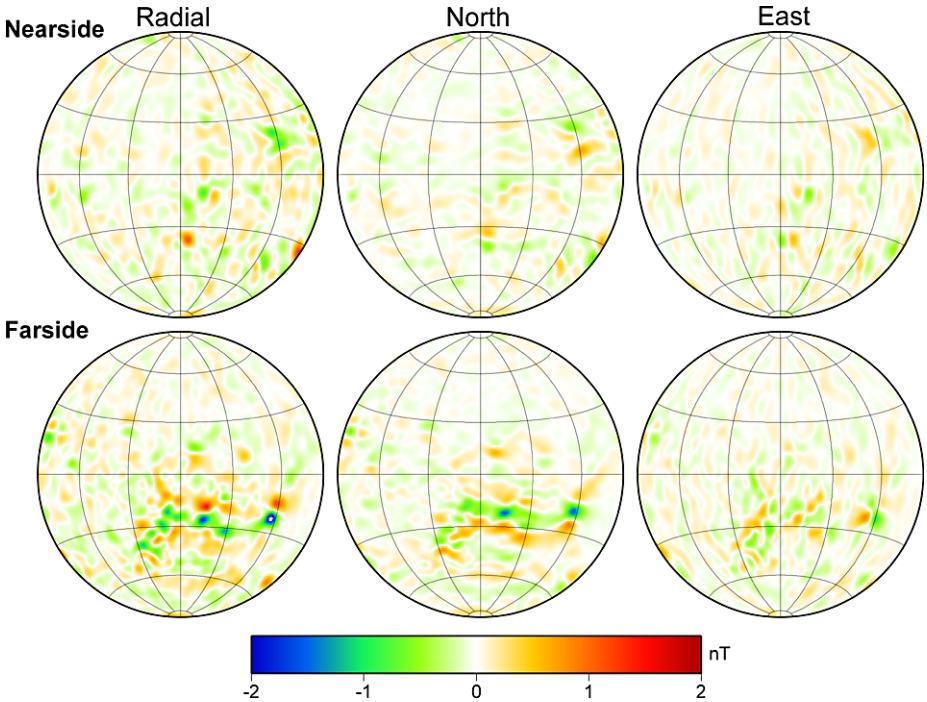

Fig. 10 Three components of the lunar magnetic anomaly normalized to a constant altitude of 100 km by applying the equivalent pole reduction (EPR) method to the Kaguya 1° × 1° bin data (Fig. 8) are shown in the ME coordinates

visualized in Fig. 11b. It is noted that we refer the basic information of the lunar basins to Wilhelms (1984) in the following description of near-basin magnetic anomalies.

4.3 Basin Antipode Regions

The Crisium antipode region (CA in Fig. 11a) near the Gerasimovic crater on the farside shows the strongest anomaly of ∼2.4 nT at 100 km altitude. This locality is consistent with the RH08 total force map (Fig. 11b). Its radial component (B_r) is positive at the northern area and negative at the southern area (Fig. 10), which agrees with the LP vector maps (see Fig. 8 by Richmond and Hood 2008). The north component (B_n) and east component (B_e) also show a good agreement with the RH08 vector maps. Although the RH08 total force maps at 30 km altitude indicate a few sharp peaks of the total force in the Crisium antipode region, the present results show only a single broader peak. This difference is probably due to the higher altitude of Kaguya.

The Serenitatis antipode region on the farside (SA) consists of a few peaks of the total force (Fig. 11a), one of which is second in the total force (∼1.8 nT) at 100 km altitude. Along 165° W longitude, there is a pair of strong B_r peaks, one positive in the north and one negative in the south at ∼10 degree distance (Fig. 10). At the center of these peaks, a strong negative peak of B_n is recognized in association with two broad peaks of positive B_n. These patterns can be explained by a south-north elongated magnetic body of northward magnetization. However, this source model is not conclusive since a positive B_r peak is unclear on the LP vector maps by Richmond and Hood (2008).

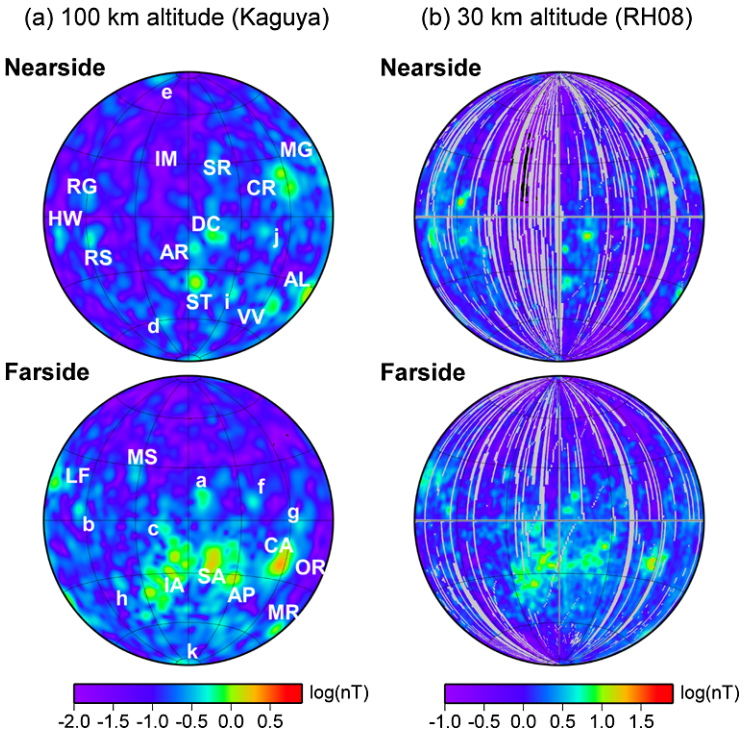

Fig. 11 Total force of the lunar magnetic anomaly calculated from three components at 100 km altitude by applying the EPR method to the Kaguya observations (**a**), and the total force at 30 km altitude by Richmond and Hood (2008) averaged for 1° × 1° bin (**b**). The *color scale* is logarithmic. *Gray color in the right* denotes vacant bins with no data

The Imbrium antipode region (IA) shows a large-scale anomaly cluster in Fig. 11a like previous works (Richmond and Hood 2008; Mitchell et al. 2008; Purucker 2008). There are several peaks of the total force in this region, and patterns of three components are complicated in association with short-wavelength anomalies (∼5 degree in length; Fig. 10) unlike the Serenitatis antipode region. These complicated signatures are consistent with the RH08 vector maps except for fine structures, so that they are not artifacts due to external field fluctuations as illustrated by Richmond and Hood (2008). It is worth noting that the Imbrium antipode anomaly cluster is weaker than the Serenitatis antipode anomaly at 100 km altitude (Fig. 11a), while it is stronger at 30 km altitude (Fig. 11b) and on the surface by the electron reflectometry (Mitchell et al. 2008). Such a rapid decrease in the anomaly intensity of the Imbrium antipode region is also seen on the 40 km altitude maps by Richmond and Hood (2008). This altitude dependence may be caused by the dominance of short-wavelength components in the Imbrium antipode region.

The Orientale antipode region is located in the Marginis basin (MG) with a center of (20° N, 84° E) and a diameter of ∼600 km, where some vague anomalies are recognized on the nearside in Fig. 11a. A stronger anomaly of ∼1 nT is seen at (16° N, 95° E) near the Marginis basin, which may belong to the Lomonosov-Fleming basin (LF) with a center of (19° N, 105° E) and a diameter of ∼600 km on the farside. This locality is consistent with the RH08 total force map (Fig. 11b) and the electron reflectometry map (Mitchell et al. 2008).

4.4 Basin Regions

The Crisium basin (CR) is located at (18° N, 59° E) with an innermost ring diameter of ∼400 km. There are two total force peaks of ∼1 nT near the northern and southern edges of the basin (Fig. 11a), which are consistent with the RH08 result (Fig. 11b). Three component distributions are different between these northern and southern intensity peaks. For example, radial components are dominated by a positive one around the northern intensity peak, while they are represented by a pair of positive and negative ones around the southern intensity peak (Fig. 10). Thus it seems difficult to explain these two anomalies by a single source of uniformly magnetized body.

The Moscoviense basin (MS) is located at (27° N, 148° E) with a diameter of ∼300 km on the farside, showing a weak and broad anomaly intensity of ∼0.4 nT (Fig. 11a) as in the RH08 total force map (Fig. 11b). The age of this basin has been considered Nectarian, that is, ∼4 billion years ago. However, the recent observation by Kaguya indicates that surface of the eastern mare basalt shows lower crater density and its age is estimated to be ∼2.5 billion years (Haruyama et al. 2009). There seem to be two peaks in Fig. 11a as in the Crisium basin anomaly. Since their intensities are small, it is not conclusive.

An isolated anomaly of ∼1 nT intensity is seen near the center of the Mendel-Rydberg basin (MR) with a center of (50° S, 94° W) and a diameter of ∼400 km on the farside. This anomaly is recognized in Fig. 11b and more clearly in the total force map by Richmond and Hood (2008). Three component distributions may be explained by a single dipole source of upward oriented magnetization (Fig. 10).

A strong anomaly of ∼1.4 nT total force is seen at the northern edge of the Apollo basin (AP) with a center of (36° S, 151° W) and a diameter of ∼500 km on the farside. This anomaly is located in the southeast of the Serenitatis antipode region. Distributions of three components are similar to those of the Serenitatis antipode anomaly. Since the Apollo basin anomaly is much weaker than the Serenitatis antipode anomaly on the RH08 total force map, it seems to constitute a part of the Serenitatis antipode anomaly cluster (Fig. 11b).

The Imbrium basin with a center of (33° N, 18° W) and a diameter of ∼1200 km shows low intensity in Fig. 11a, as indicated by previous works (Richmond and Hood 2008; Mitchell et al. 2008; Purucker 2008). In the Orientale basin with a center of (20° S, 95° W) and a diameter of ∼900 km, there is almost no anomaly in Fig. 11a. This feature is consistent with the mapping results by Mitchell et al. (2008) and Purucker (2008), although the RH08 total force map seems to show very weak anomalies due to external field fluctuations (Fig. 11b). In the Serenitatis basin with a center of (27° N, 19° E) and a diameter of ∼700 km, there seems to be a weak and broad anomaly of ∼0.4 nT near the center (Fig. 11a). A weak anomaly cluster may be recognized in the Serenitatis basin on the RH08 total force map (Fig. 11b), although its intensity seems comparable to the noise level.

4.5 Other Isolated Anomalies

Richmond and Hood (2008) reported other strong isolated anomalies on the nearside: Reiner Gamma (RG), Rima Sirsalis (RS), Hartwig (HW), Decartes (DC), Airy (AR), Stöfler (ST), Abel (AL) and Vallis Snellis and Vallis Rheito (VV). All of them are identified almost at the same localities on the 100 km map of the total force by Kaguya (Fig. 11a).

There seem to be more anomalies on both the nearside and farside on the 100 km total force map (Fig. 11a) as shown by symbols of *a*–*k*. Broad anomaly *a* at (15° N, 170° W) on the farside corresponds to two anomalies on the 30 km total force map of RH08 (Fig. 11b). Anomaly *b* at (5° N, 115° E) on the farside is recognized to be an isolated one at the same

locality in Fig. 11b. Anomaly *c* at (5° S, 165° E) near the Keeler-Heaviside basin on the farside is found to be a small cluster-like anomaly in Fig. 11b. Anomaly *d* at (60° S, 25° W) on the nearside is weak and small in Fig. 11a, and it may correspond to a weaker and smaller one at the same locality in Fig. 11b. Anomaly *e* is located at (70° N, 65° W) near the north pole on the nearside, and a weak anomaly is seen at the same locality in Fig. 11b. These anomalies of *a*–*e* are more clearly identified as small but strong anomalies of more than 3 nT on the total force map at 30 km altitude by Richmond and Hood (2008; see Fig. 7a). The agreement of *a*–*e* anomalies between two different datasets indicates that these weak and small anomalies are not artifacts. Anomalies of *f*–*k* are also found on the 100 km-altitude map (Fig. 11a). Although there seem to be anomalies at the same localities on the 30 km-altitude map (Fig. 11b), they are less recognizable.

5 Discussion on the Lunar Crustal Magnetism

5.1 Weak Magnetic Anomalies over the Lunar Surface

The results of mapping magnetic anomalies in the present study well agree with previous studies using the LP data with respect to the isolated weak anomalies of $\leq$1 nT at 100 km altitude as well as strong ones. This agreement between the different datasets indicates that the weak magnetic anomalies are originated from the lunar crustal magnetization and suggests that the Kaguya observations precisely detected weak magnetic anomaly fields. Thus we check weaker anomaly fields of the lunar crustal magnetism, while the strong magnetic anomalies have attracted us so far.

The present study provides a dataset of magnetic anomalies at $\sim$100 km altitude. However, the 100 km-altitude maps are not suitable to the analysis of relatively weak and small-size anomalies, since those anomaly fields are subject to extensive attenuation in amplitudes at high altitude. As indicated in the previous section, the Imbrium antipode (IA) anomaly cluster is weaker than the Serenitatis antipode (SA) anomaly at 100 km altitude (Fig. 11a), while this relationship is reversed at 30 km altitude (Fig. 11b). This rapid decrease of the IA anomaly field in intensity is probably caused by its complicated features of magnetic anomalies resulting in dominance of short-wavelength components. Thus we use the surface density map of equivalent poles (Fig. 12a), which is regarded as the distribution of $2B_r$ on the surface (see Sect. 3.4.1). The error is estimated to be $\pm$0.48 nT for the equivalent pole distribution, that is, $\pm$0.24 nT for the surface B_r. This equivalent pole density map is compared with B_r of the RH08 map at 30 km altitude (Fig. 12b). Richmond and Hood (2008) do not explicitly show anomaly fields of smaller amplitudes than 1 nT for three components, while Purucker (2008) mapped magnetic anomalies over the lunar surface using the LP dataset. In order to obtain a clear view of weak anomalies, smaller full scales are adopted in Figs. 12a and b.

It is seen that the equivalent pole density on the surface shows large amplitudes in the Imbrium antipode region while there are only very weak signatures in the Orientale basin (Fig. 12a). There are many weak but significant anomalies of 10–20 degree wavelength over most of the lunar surface except for the Orientale and Imbrium basin regions (Figs. 12a and b). It is striking in Figs. 12a and b that fine structures of strong and weak anomalies are similar on both maps over most of the lunar surface, although the equivalent pole distribution shows slightly smoother patterns than the B_r distribution of the LP map at 30 km altitude. The reason for this smoothness is probably that signatures of very short wavelength components at 100 km altitude are contaminated with noise and reduced through the smoothing effect of the EPR procedure (see Sect. 3.4.2).

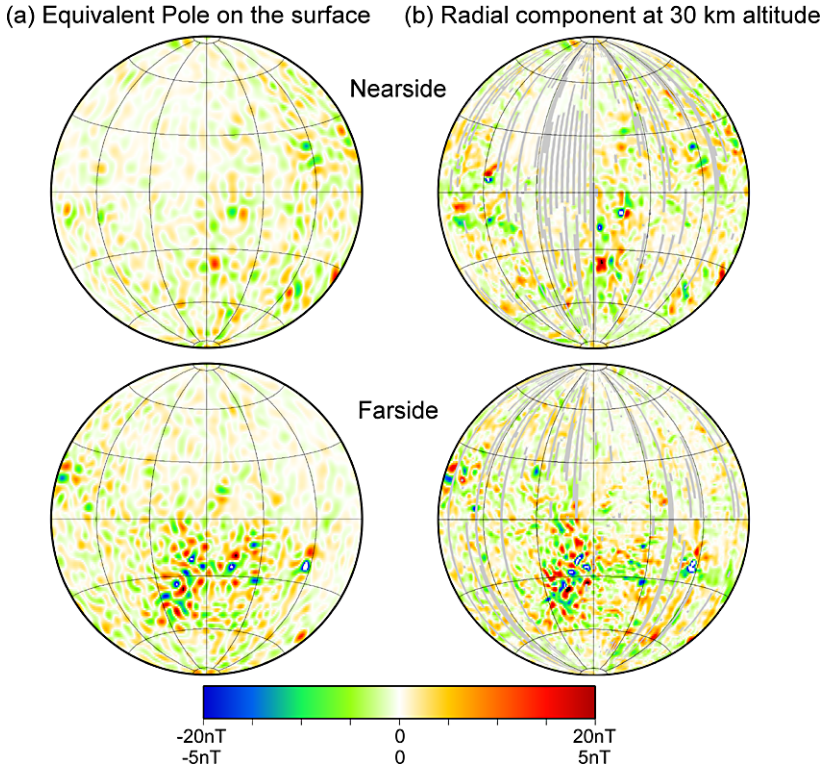

Fig. 12 The surface density of equivalent poles from the Kaguya observations and the radial component at a 30 km altitude from the Lunar Prospector observations (Richmond and Hood 2008). *Lower* and *upper color scales* correspond to the maps from the Kaguya and Lunar Prospector datasets, respectively. It is noted that equivalent pole density is approximated to be twice the surface radial component. *Gray color in the right* denotes vacant bins with no data. *White part* denotes values out of the full scale

The surface B_r value is approximated to be half of the equivalent pole density, and its mean value is calculated in a one-degree bin of the low-to-middle latitude region (60° S–60° N). B_r values of the RH08 dataset at 30 km altitude are also averaged for the same bins. Comparing those values, a correlation coefficient is calculated to be 0.394. Taking mean values of B_r in a six-degree bin to average out very short wavelength components, a correlation coefficient is 0.615 with a slope of 1.44 and an intercept of −0.02 (Fig. 13). Nearly null intercept indicates no systematic offset between these B_r distributions, and the slope is attributed to the attenuation depending on wavelength. If n-degree component of spherical harmonics ($B_{n,r}$) is representative of the weak anomalies, the altitude dependence is given by the following equation from (3.16),

$$B_{n,r}(\boldsymbol{r}) = \frac{1}{n+1}\left(\frac{R}{r}\right)^{n+2} Y_n(\theta, \varphi),$$

and the representative degree n is

$$n = \ln(1/1.44)/\ln(1738.4/1768.4) - 2 \approx 19,$$

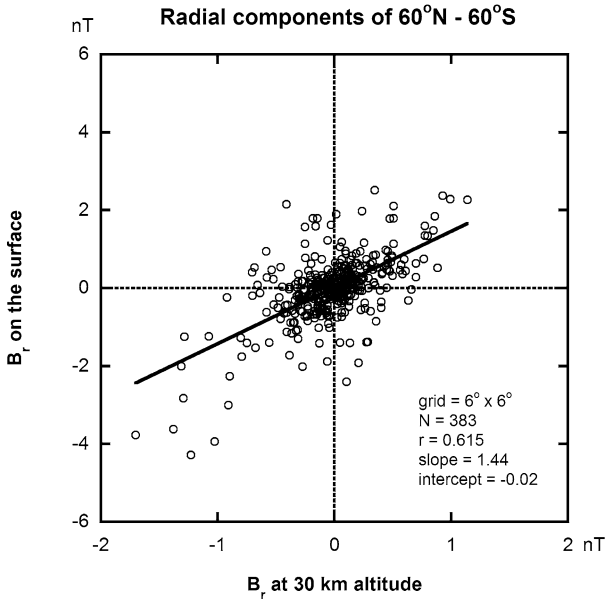

Fig. 13 Correlation diagram of the radial component between values on the surface and at 30 km altitude. The surface values were calculated from the equivalent pole density from the Kaguya dataset, while the 30 km altitude values were calculated from the Lunar Prospector dataset prepared by Richmond and Hood (2008). *Each point* indicates a value averaged for $6° \times 6°$ bin. If a six-degree bin includes a vacant one-degree bin in Fig. 12b or shows an averaged value of $|B_r| > 2$ nT, such a bin is not used. It is noted that the number of bins of $|B_r| > 2$ nT is two ($N = 2$)

19-degree spherical harmonic term has a wavelength of ∼18.6 degree (∼565 km), which is concordant with the dominant wavelength of B_r in Figs. 12a and b as mentioned above. Therefore it is indicated that weak anomalies over most of the lunar surface are not artifacts but likely to be originated from the lunar crustal magnetization.

5.2 Ambient Field Inducing the Lunar Crustal Magnetization

According to the basin-forming impact model (e.g. Lin et al. 1988), the interplanetary magnetic field (IMF) around the Moon is pushed toward an antipode of the impact area and piled up there. The field intensity at the antipode area becomes strong enough to yield shock remanence due to deposition of the impact ejecta. That process is likely to explain strong magnetic anomalies in the basin-antipode regions. In particular, the Crisium antipode region (CA) associated with no remarkable topographical features and gravity anomalies (Fig. 14) suited to be elucidated by the basin-forming model. However, that model seems to have difficulty explaining weak anomalies over the lunar surface and the magnetic anomalies in the near-basin and near-crater regions.

As pointed out in Sect. 1, the lunar magnetic anomalies should be studied for two major problems: one is an ambient field inducing significant remanence intensity and the other is a type of remanence of the anomaly source. If the IMF of ∼10 nT is an ambient field inducing the remanence, it should be enhanced extensively by some mechanism like the basin-forming model. However, it seems difficult to amplify IMF over the lunar surface to yield widely-distributed anomalies. This difficulty is settled if a global magnetic field of the early lunar dynamo is assumed. A recent study of the numerical dynamo simulation shows that an early lunar dynamo could exist in association with dichotomy of thermal condition at the lunar core-mantle boundary (Takahashi and Tsunakawa 2009). They suggest that such an ancient lunar dynamo could have a dipolar field of more than 100 nT, possibly 1 μT, on the lunar surface with polarity reversals and that the lunar crustal magnetization would be acquired in an early lunar magnetosphere. For the strong magnetic anomalies, the dynamo

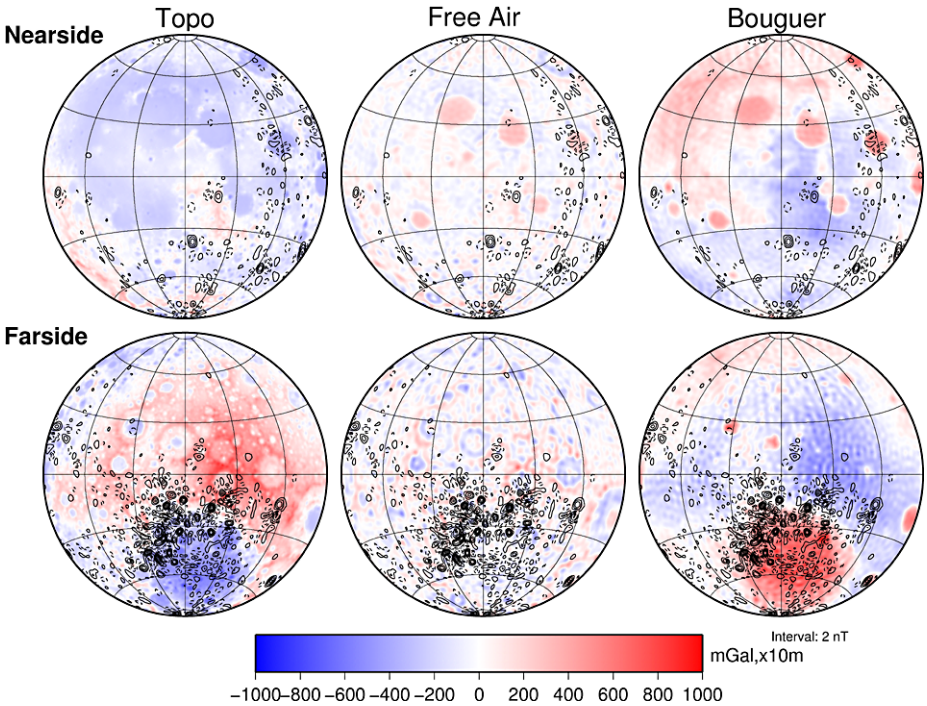

Fig. 14 Maps for correlation of the radial component distribution with the topography, the free-air gravity anomaly and the Bouguer gravity anomaly. The radial component is mapped at 2 nT intervals (*solid line*, positive; *dashed line*, negative). The distributions of the topography, the free-air gravity anomaly and the Bouguer gravity anomaly are referred to the public database of the SELENE (Kaguya) data archives

field is also one of the possible ambient fields enhanced by the basin-forming impact (Hood and Artemieva 2008). It is worth noting that, if the ancient lunar dynamo ceased before the Orientale basin formation, which is considered to be the youngest basin on the Moon, the basin and its surrounding rocks could be demagnetized (e.g. Mitchell et al. 2008).

5.3 Global Correlations of the Anomaly Distribution with Other Data

The other problem is a type of remanent magnetization of the anomaly source, which is tightly linked to mechanism of the magnetization acquisition. It is meaningful to examine a global-scale correlation of the magnetic anomaly distribution with other mapping results. We roughly check its correlation with the lunar surface topography, free-air, and Bouguer gravity anomalies in Fig. 14. The anomaly field is represented here by the surface B_r as half of the equivalent pole density, while the topography, free-air, and Bouguer gravity anomalies are mapped on the basis of the recent public database of the SELENE (Kaguya) data archives (e.g. Araki et al. 2009; Namiki et al. 2009). If the impact-origin magnetic anomaly dominates, there should be a good correlation of B_r with the topography and/or the free air anomaly. If magnetized bodies of extrusive or intrusive rocks carry most of the crustal magnetization, the locality of the magnetic anomaly should be well correlated with the topography and/or the Bouguer anomaly distribution. It is seen that many magnetic anomalies are concentrated at the northwestern edge of the South-Pole Aitken basin as pointed out by previous studies (e.g. Richmond and Hood 2008;

Mitchell et al. 2008). However, there seems to be no other clear correlation on a global scale (Fig. 14) implying that the lunar magnetic anomalies may not be attributed to a single magnetization process.

5.4 Remanence Type and Direction of the Lunar Crust Magnetization

Most of the previous studies have concentrated on the anomaly intensity. It is known that the magnetization intensity depends on not only the ambient field intensity but also the configuration of anomaly sources such as an edge effect and the rock magnetic property of anomaly sources such as a remanence type and a magnetic mineral content. However, it seems difficult to accurately determine the source configuration and the rock magnetic property from the remote sensing data. This problem is more serious if the anomaly source is buried and covered by the surface material. The laboratory experiment of lunar rocks is useful for the rock magnetic study but not easy, since their magnetic minerals are composed of iron metal, unlike the Earth's rocks. These difficulties can possibly cause overestimation or underestimation of the ambient field intensity recorded in lunar rocks.

The magnetization direction is also important in understanding crustal magnetization. As mentioned in Sect. 4, the main anomaly in the Serenitatis antipode region is possibly interpreted to have a source of northward magnetized body. There is, however, a fundamental problem whether possible remanences of the lunar crustal rock can accurately record the ambient magnetic field.

From the rock magnetic study of lunar rocks, two possible remanences have mainly been proposed: thermoremanent magnetization (TRM) and shock remanent magnetization (SRM). TRM is acquired when crustal rocks are formed in magmatic process and cooled below the Curie temperature (T_c) of magnetic minerals and further below their blocking temperatures. According to the rock magnetic study, lunar rocks mostly contain kamacite, Fe–Ni alloy of $T_c \sim 770°C$ (e.g. Fuller 1974). TRM satisfies the parallel and proportional laws, recording the ambient field precisely. SRM is gained when crustal rocks undergo a shock event with hypervelocity (e.g. Nagata 1971; Cisowski and Fuller 1978). A recent experiment shows that SRM possibly has the parallelism and proportionality to the ambient field (Gattacceca et al. 2008). In addition to SRM, a shock event may induce piezoremanent magnetization (PRM) in relatively lower pressure and TRM by heating up to blocking temperatures (e.g. Gattacceca et al. 2007). PRM is possibly parallel to the ambient field and effective on lower coercivity part of magnetic minerals (e.g. Kinoshita 1968). Although experiments of kamacite have not been sufficient, the above crustal magnetizations could record the ambient field, in particular, its direction. This may enable us to obtain the information of the ambient field at the time of magnetization acquisition regardless of the remanence type.

If lunar crustal rocks around a basin antipode are remagnetized under an ambient field extensively deformed by the basin-forming impact, their magnetization directions are expected to be nearly vertical (e.g. Hood and Artemieva 2008). If lunar crustal magnetizations are acquired in a dipolar dynamo field without deformation, their magnetic poles should be concentrated like the geomagnetic field. Previous studies of the Apollo data may suggest a few concentrated areas of magnetic poles (e.g. Runcorn 1983), however, the coverage of the Apollo observations is limited to the low-to-middle latitude region. Since the lunar magnetic anomalies possibly have multiple origins, anomaly clusters, isolated strong and weak anomalies, and widely-distributed weak anomalies should be classified and analyzed with careful consideration of their morphological characteristics and ages like the paleomagnetism of the Earth.

The analysis of the magnetization direction needs some assumption of source configuration such as a dipole and disk. Using the LP datasets at two different altitudes, Kurata et al. (2005) show that two isolated anomalies in the Reiner Gamma region are well approximated with two corresponding dipole sources at ∼10 km depth. Based on the global observation at low altitudes by Kaguya together with that by Lunar Prospector, precise analyses of magnetization directions will provide insight into lunar crustal magnetism.

6 Conclusions

(1) We have developed and calibrated the lunar magnetometer (LMAG) onboard Kaguya and successfully observed the lunar magnetic field for a nominal altitude of ∼100 km for about 14 months. Signals of the lunar magnetic anomaly were extracted and mapped, applying the new technique of the Bayesian procedure. As a result, initial global maps of the lunar magnetic anomaly in $1^\circ \times 1^\circ$ bins were obtained with 95% coverage of the lunar surface with an error level of ±0.1 nT.
(2) Observations of the magnetic field due to the crustal magnetization at different altitudes are reduced to scalar boundary values on the lunar surface such as the potential, radial magnetic field and magnetic charge. This procedure is mathematically defined as three types of the inverse boundary value problem. Once a boundary value distribution is obtained, the anomaly field can be calculated at an arbitrary point above the surface.
(3) The equivalent pole reduction (EPR) method corresponds to the Cauchy type of the inverse boundary value problem, and its density distribution is approximated to be twice the radial component of the surface magnetic field. Applying the EPR method to the Kaguya-LMAG bin data at ∼100 km altitude, full-coverage magnetic anomaly maps were obtained at a constant altitude of 100 km with an error level of ±0.2 nT.
(4) Characteristic features of the mapping results in the present study agree with those of the Lunar Prospector with respect to not only the strong anomalies at basin-antipode regions but also weaker isolated anomalies. Thus the Kaguya-LMAG maps give reliable vector fields of the lunar crustal magnetization at 100 km altitude.
(5) Striking is the consistency of widely-distributed weak anomalies between the Kaguya and Lunar Prospector observations. This suggests that most regions of the lunar crust are magnetized except for a few parts such as the Orientale basin. It seems that the lunar crustal magnetization might be acquired in a global magnetic field, possibly, due to the ancient lunar dynamo.

Acknowledgements The authors wish to express their sincere thanks to all of the SELENE team members, especially to Yukiko Yokoyama, Chizu Itota, Naoto Oshiman, Hirokuni Oda, Yuhji Yamamoto, Nobutatsu Mochizuki and Naoki Horii for their help with the ground test, and to Hirokazu Hoshino, Jun Kimura, Hironori Maejima, Hayato Okumura, Shin-ichi Sobue, Koji Tanaka, Naoki Tateno and Yukio Yamamoto for help during the observation. We are also grateful to Takanobu Omoto at Meisei Electric Co. and Yoshinari Takeuchi at NIPPI Co. for great support in developing the instrument. Masahiro Toyoshima and Aya Hayashida are grateful for their help in the EPR analysis. MAP-PACE team is especially appreciated for the collaboration of the SELENE project.

References

H. Akaike, Likelihood and the Bayes procedure, in *Bayesian Statistics*, ed. by J.M. Bernardo et al. (1980), pp. 143–166

H. Araki, S. Tazawa, H. Noda, Y. Ishihara, S. Goossens, S. Sasaki, N. Kawano, I. Kamiya, H. Otake, J. Oberst, C. Shum, Lunar global shape and polar topography derived from KAGUYA-LALT laser altimetry. Science **323**, 897–900 (2009). doi:10.1126/science.1164146

S. Cisowski, M. Fuller, The effect of shock on the magnetism of terrestrial rocks. J. Geophys. Res. **83**, 3,441–3,458 (1978)

P.J. Coleman, C.T. Russell, L.R. Sharp, G. Schubert, Preliminary mapping of the lunar magnetic field. Phys. Earth Planet. Inter. **6**, 167–174 (1972)

P. Dyal, C.W. Parkin, W.D. Daily, Magnetism and the interior of the Moon. Rev. Geophys. Space Phys. **12**, 568–591 (1974)

M. Fuller, Lunar Magnetism. Rev. Geophys. **12**, 23–70 (1974)

I. Garric-Bethell, P.W. Benjamin, L.S. David, B. Jennifer, Early lunar magnetism. Science **323**, 356–359 (2009)

J. Gattacceca, A. Lamalib, P. Rochettea, M. Boustiec, L. Berthed, The effects of explosive-driven shocks on the natural remanent magnetization and the magnetic properties of rocks. Phys. Earth Planet. Inter. **162**, 85–98 (2007). doi:10.1016/j.pepi.2007.03.006

J. Gattacceca, L. Berthe, M. Boustie, F. Vadeboin, P. Rochette, T. De Resseguier, On the efficiency of shock remanent processes. Phys. Earth Planet. Inter. **166**, 1–10 (2008). doi:10.1016/j.pepi.2007.09.005

J.S. Halekas, D.L. Mitchell, R.P. Lin, S. Frey, L.L. Hood, M.H. Acuña, A.B. Binder, Mapping of crustal magnetic anomalies on the lunar near side by the Lunar Prospector electron reflectometer. J. Geophys. Res. **106**, 27,841–27,852 (2001)

J.S. Halekas, S.D. Bale, D.L. Mitchell, R.P. Lin, Electrons and magnetic fields in the lunar plasma wake. J. Geophys. Res. **110**, A07222 (2005)

J.S. Halekas, D.A. Brain, D.L. Mitchell, R.P. Lin, L. Harrison, On the occurrence of magnetic enhancements caused by solar wind interaction with lunar crustal fields. Geophys. Res. Lett. **33**, L08106 (2006)

J.S. Halekas, G.T. Delory, D.A. Brain, R.P. Lin, D.L. Mitchell, Density cavity observed over a strong lunar crustal magnetic anomaly in the solar wind: a mini-magnetosphere? Planet. Space Sci. **56**, 941–946 (2008)

W.K. Hartmann, D.R. Davis, Satellite-sized planetesimals and lunar origin. Icarus **24**, 505 (1975)

J. Haruyama, M. Ohtake, T. Matsunaga, T. Morota, C. Honda, Y. Yokota, M. Abe, Y. Ogawa, H. Miyamoto, A. Iwasaki, C.M. Pieters, N. Asada, H. Demura, N. Hirata, J. Terazono, S. Sasaki, K. Saiki, A. Yamaji, M. Torii, J.-L. Josset, Long-lived volcanism on the lunar farside revealed by SELENE Terrain Camera. Science **323**, 905–908 (2009). doi:10.1126/science.1163382

L.L. Hood, N.A. Artemieva, Antipodal effects of lunar basin forming impacts: initial 3D simulations and comparisons with observations. Icarus **193**, 485–502 (2008)

L.L. Hood, A. Vickery, Magnetic field amplification and generation in hypervelocity meteoroid impacts with application to lunar paleomagnetism. J. Geophys. Res. **89**, C211–C223 (1984) (suppl.)

L.L. Hood, C.T. Russell, P.J. Coleman Jr., Contour maps of the lunar remanent magnetic fields. J. Geophys. Res. **86**, 1055–1069 (1981)

L.L. Hood, D.L. Mitchell, R.P. Lin, M.H. Acuna, A.B. Binder, Initial measurements of the lunar induced magnetic dipole moment using Lunar Prospector magnetometer data. Geophys. Res. Lett. **26**, 2327–2330 (1999)

L.L. Hood, A. Zakharian, J. Halekas, D.L. Mitchell, R.P. Lin, M.H. Acuña, A.B. Binder, Initial mapping and interpretation of lunar crustal magnetic anomalies using Lunar Prospector magnetometer data. J. Geophys. Res. **106**, 27,825–27,839 (2001)

J.D. Jackson, *Classical Electrodynamics*, 3rd edn. (Wiley, New York, 1998), p. 808

H. Kinoshita, Studies on piezo-magnetization (III)-PRM and relating phenoma. J. Geomagn. Geoelectr. **20**, 155–167 (1968)

S. Kokubun, T. Yamamoto, M.H. Acuña, K. Hayashi, K. Shiokawa, H. Kawano, The Geotail magnetic field experiment. J. Geomagn. Geoelectr. **46**, 7–21 (1994)

M. Kurata, H. Tsunakawa, Y. Saito, H. Shibuya, M. Matsushima, H. Shimizu, Mini-magnetosphere over the Reiner Gamma magnetic anomaly region on the Moon. Geophys. Res. Lett. **32**, L24205 (2005). doi:10.1029/2005GL024097

R.A. Langel, An investigation of a correlation/covariance method of signal extraction. J. Geophys. Res. **100**, 20137–20157 (1995)

R.P. Lin, K.A. Anderson, L.L. Hood, Lunar surface magnetic field concentrations antipodal to young large impact basins. Icarus **74**, 529–541 (1988)

R.P. Lin, D.L. Mitchell, D.W. Curtis, K.A. Anderson, C.W. Carlson, J. McFadden, M.H. Acuña, L.L. Hood, A.B. Binder, Lunar surface magnetic fields and their interaction with the solar wind: results from Lunar Prospector. Science **281**, 1480–1484 (1998)

E.F. Lyon, H.S. Bridge, J.H. Binsack, Explorer 35 plasma measurements in the vicinity of the Moon. J. Geophys. Res. **72**, 6113–6117 (1967)

M. Matsushima, H. Tsunakawa, Y. Iijima, S. Nakazawa, A. Matsuoka, S. Ikegami, T. Ishikawa, H. Shibuya, H. Shimizu, F. Takahashi, Magnetic cleanliness program under control of electromagnetic compatibility for the SELENE (Kaguya) spacecraft. Space Sci. Rev. (2010, this issue)

D.L. Mitchell, J.S. Halekas, R.P. Lin, S. Frey, L.L. Hood, M.H. Acuña, A.B. Binder, Global mapping of lunar crustal magnetic fields by Lunar Prospector. Icarus **194**, 401–409 (2008)

T. Nagai, H. Tsunakawa, H. Shibuya, F. Takahashi, H. Shimizu, M. Matsushima, M.N. Nishino, Y. Saito, O. Amm, Plasmoid formation for multiple onset substorms: observations of the Japanese lunar mission "Kaguya". Ann. Geophys. **27**, 59–64 (2009)

T. Nagata, Introductory notes on shock remanent magnetization and shock demagnetization of igneous rocks. Pure Appl. Geophys. **89**, 159–177 (1971)

T. Nakagawa, F. Takahashi, H. Tsunakawa, H. Shibuya, H. Shimizu, M. Matsushima, Non-monochoromatic whistler waves detected by Kaguya on the dayside surface of the Moon. Earth Planets Space (2010, in press)

N. Namiki, T. Iwata, K. Matsumoto, H. Hanada, H. Noda, S. Goossens, M. Ogawa, N. Kawano, K. Asari, S. Tsuruta, Y. Ishihara, Q. Liu, F. Kikuchi, T. Ishikawa, S. Sasaki, C. Aoshima, K. Kurosawa, S. Sugita, T. Takano, Farside gravity field of the Moon from four-way doppler measurements of SELENE (KAGUYA). Science **323**, 900–905 (2009). doi:10.1126/science.1168029

M.N. Nishino, K. Maezawa, M. Fujimoto, Y. Saito, S. Yokota, K. Asamura, T. Tanaka, H. Tsunakawa, M. Matsushima, F. Takahashi, T. Terasawa, S. Shibuya, H. Shimizu, Pairwise energy gain-loss feature of solar wind protons in the near-Moon wake. Geophys. Res. Lett. **36**, L12108 (2009a). doi:10.1029/2009GL039049

M.N. Nishino, M. Fujimoto, K. Maezawa, Y. Saito, S. Yokota, K. Asamura, T. Tanaka, H. Tsunakawa, M. Matsushima, F. Takahashi, T. Terasawa, H. Shibuya, H. Shimizu, Solar-wind proton access deep into the near-Moon wake. Geophys. Res. Lett. **36**, L16103 (2009b). doi:10.1029/2009GL039444

M.E. Purucker, A global model of the internal magnetic field of the Moon based on Lunar Prospector magnetometer observations. Icarus **197**, 19–23 (2008). doi:10.1016/j.icarus.2008.03.16

N.C. Richmond, L.L. Hood, A preliminary global map of the vector lunar crustal magnetic field based on Lunar Prospector magnetometer data. J. Geophys. Res. **113**, E02010 (2008). doi:10.1029/2007JE002933

G.F. Roach, *Green's Functions*, 2nd edn. (Cambridge University Press, Cambridge, 1982), p. 325

S.K. Runcorn, Lunar magnetism, polar displacements and primeval satellites in the Earth–Moon system. Nature **304**, 589–596 (1983)

Y. Saito, S. Yokota, K. Asamura, T. Tanaka, R. Akiba, M. Fujimoto, H. Hasegawa, H. Hayakawa, M. Hirahara, M. Hoshino, S. Machida, T. Mukai, T. Nagai, T. Nagatsuma, M. Nakamura, K. Oyama, E. Sagaw, S. Sasaki, K. Seki, T. Terasawa, Low energy charged particle measurement by MAP-PACE onboard SELENE. Earth Planets Space **60**, 375–386 (2008a)

Y. Saito, S. Yokota, T. Tanaka, K. Asamura, M. Nishino, M. Fujimoto, H. Tsunakawa, H. Shibuya, M. Matsushima, H. Shimizu, F. Takahashi, T. Mukai, T. Terasawa, Solar wind proton reflection at the lunar surface: low energy ion measurement by MAP-PACE onboard SELENE (KAGUYA). Geophys. Res. Lett. **35**, L24205 (2008b). doi:10.1029/2008GL036077

Y. Saito, S. Yokota, T. Tanaka, K. Asamura, M.N. Nishino, T. Yamamoto, H. Tsunakawa, H. Shibuya, H. Shimizu, F. Takahashi, M. Matsushima, Lunar plasma measurement by MAP-PACE onboard KAGUYA (SELENE). Eos Trans. Am. Geophys. Union, Fall Meet. Suppl. **89**(53), P51D-02 (2008c)

Y. Saito, S. Yokota, K. Asamura, T. Tanaka, M.N. Nishino, T. Yamamoto, Y. Terakawa, M. Fujimoto, H. Hasegawa, H. Hayakawa, M. Hirahara, M. Hoshino, S. Machida, T. Mukai, T. Nagai, T. Nagatsuma, T. Nakagawa, M. Nakamura, K. Oyama, E. Sagawa, S. Sasaki, K. Seki, I. Shinohara, T. Terasawa, H. Tsunakawa, H. Shibuya, M. Matsushima, H. Shimizu, F. Takahashi, In-flight performance and initial results of Plasma energy Angle and Composition Experiment (PACE) on SELENE (Kaguya). Space Sci. Rev. (2010, this issue)

P.H. Schultz, L.J. Srnka, Cometary collisions with the Moon and Mercury. Nature **284**, 22–26 (1980)

H. Shimizu, F. Takahashi, N. Horii, A. Matsuoka, M. Matsushima, H. Shibuya, H. Tsunakawa, Ground calibration of the high-sensitivity SELENE lunar magnetometer LMAG. Earth Planets Space **60**, 353–363 (2008)

D.R. Stegman, A.M. Jellinek, S.A. Zatman, J.R. Baumgardner, M.A. Richards, An early lunar core dynamo driven by thermochemical mantle convection. Nature **421**, 143–146 (2003)

F. Takahashi, H. Shimizu, M. Matsushima, H. Shibuya, A. Matsuoka, S. Nakazawa, Y. Iijima, H. Otake, H. Tsunakawa, In-orbit calibration of the lunar magnetometer onboard SELENE (KAGUYA). Earth Planets Space **61**, 1269–1274 (2009)

F. Takahashi, H. Tsunakawa, Thermal core-mantle coupling in an early lunar dynamo: implications for a global magnetic field and magnetosphere of the early Moon. Geophys. Res. Lett. **36**, L24202 (2009). doi:10.1029/2009GL041221

T. Tanaka, Y. Saito, S. Yokota, K. Asamura, M.N. Nishino, H. Tsunakawa, H. Shibuya, M. Matsushima, H. Shimizu, F. Takahashi, M. Fujimoto, T. Mukai, T. Terasawa, First in-situ observation of the Moon-originating ions in the Earth's magnetosphere by MAP-PACE on SELENE (KAGUYA). Geophys. Res. Lett. **36**, L22106 (2009). doi:10.1029/2009GL040682

M. Toyoshima, H. Shibuya, M. Matsushima, H. Shimizu, H. Tsunakawa, Equivalent source mapping of the lunar crustal magnetic field using ABIC. Earth Planets Space **60**, 365–373 (2008)

H. Tsunakawa, Bayesian approach to smoothing palaeomagnetic data using ABIC. Geophys. J. Int. **108**, 801–811 (1992)

D.E. Wilhelms, The Moon, in *The Geology of the Terrestial Planets*, ed. by M. Carr et al. (1984) pp. 107–205

T. Yamamoto, A. Matsuoka, PLANET-B magnetic fields investigation. Earth Planets Space **50**, 189–194 (1998)

S. Yokota, Y. Saito, K. Asamura, T. Tanaka, M.N. Nishino, H. Tsunakawa, H. Shibuya, M. Matsushima, H. Shimizu, F. Takahashi, M. Fujimoto, T. Mukai, T. Terasawa, First direct detection of ions originating from the Moon by MAP-PACE IMA onboard SELENE (KAGUYA). Geophys. Res. Lett. **36**, L11201 (2009). doi:10.1029/2009GL038185